IRRADIATION INDUCED DISLOCATION CLIMB IN Cu-Al ALLOYS OF DIFFERENT STACKING FAULT ENERGIES

Contents

IRRADIATION INDUCED DISLOCATION CLIMB IN Cu-Al ALLOYS OF DIFFERENT STACKING FAULT ENERGIES

Thomas Herbert Kosel

Inorganic Materials Research Division, Lawrence Berkeley Laboratory and Department of Materials Science and Engineering, College of Engineering; University of California, Berkeley, California

ABSTRACT

Irradiation induced climb of dislocations due to preferential absorption of interstitials was studied by irradiating Cu-Al alloys of different stacking fault energies at elevated temperatures in the beam of the Hitachi 650 kV electron microscope. Nucleation of rhombus shaped perfect dislocation loops was observed, and their growth was studied at different temperatures and with different electron fluxes. The sides of the loops lay accurately on the two {111} planes which contain the Burgers vector and were often bowed out slightly on these glide planes. Rotation of the loops on the glide cylinder away from the pure edge orientation was observed, as well as loss of loops by slip along the glide cylinder to the foil surface. These observations suggest that the jog density on the loop sides is low. It is shown that at a given temperature there exists a minimum damage rate for growth, and that this is strongly dependent on stacking fault energy. This is discussed in terms of a model in which the rate controlling process in the climb of these loops is assumed to be the nucleation of jogs.

I. INTRODUCTION

A great deal of research has been done in recent years on the problem of void growth in irradiated metals.[1-24] It is generally accepted that the growth of voids by the absorption of vacancies during irradiation requires the existence in the metal of sinks which have a preferential attraction for interstitials, so that an excess of vacancies is left to diffuse to essentially unbiased sinks such as grain boundaries or free surfaces. Since interstitials have a larger strain field than do vacancies, they are more strongly affected by the strain fields around dislocations, and this should lead to an enhanced diffusion rate of interstitials to dislocations. It is generally accepted, therefore, that dislocations are the biased sinks required to explain void growth.[2,3] The enhancement of the diffusion rate of interstitials over that of vacancies by the strain field of a dislocation will lead to climb of the dislocation at a rate determined by the difference in the arrival rate of the two types of defect at the dislocation core. However, if an energy barrier exists for the process of absorption of point defects at the dislocation core, the climb rate of a dislocation may be controlled by the rate at which absorption occurs rather than by the rate of diffusion of point defects to the dislocation. Clearly, any such factors affecting the climb of dislocations are of importance in the study of irradiation induced void growth in metals. Theories of void formation in metals generally assume diffusion controlled dislocation climb (e.g., Harkness and Li[4]). In the present work evidence is presented which suggests that in metals of low stacking fault energy dislocation climb may sometimes be controlled by the rate of jog nucleation.

Most theories of irradiation creep in metals also involve mechanisms dependent on dislocation climb processes. Creep due to preferential climb of favorably oriented dislocation loops has been discussed by Ashby.[5] Preferential nucleation and growth of dislocation loops oriented so that their climb would lower the creep stress have been considered in detail by Brailsford and Bullough,[6] who concluded that preferential nucleation was more important than preferential growth. Lewthwaite[7] has also treated the preferential nucleation of favorably oriented dislocation loops. Gittus[8,9,10] has written a series of papers elaborating a theory of climb controlled glide of dislocations in which creep stresses are relieved by the climb of dislocations around obstacles. Thus, factors affecting dislocation climb are also of interest in the study of irradiation creep. Although evidence indicating the presence of internal stresses during irradiation was found in this work, these stresses were not observed to have much effect on the growth or nucleation rates of loops of different orientations. However, the observation of an activation barrier to climb in this work should be of interest in creep studies.

Voids may be produced in metals by irradiation with neutrons,[11-13,46] ions,[15-19] or electrons,[20-24] and it is useful to consider briefly the differences inherent in these irradiation techniques.[25,26] Irradiation of metals with sufficiently energetic particles results in collisions in which the incoming particle imparts sufficient energy to a metal atom to knock it out of its lattice site, leaving behind a vacancy. The metal atom displaced in this primary collision is called the primary knock-on, and the energy it absorbs is a function of the energy of the incoming particle (E_1), the masses of the incoming particle (M_1) and the metal atom (M_2), and the direction taken by the primary knock-on after the collision. The maximum energy transfer to the primary knock-on occurs for a head-on collision, and is

$$E_2 = \frac{4M_1M_2}{(M_1 + M_2)} E_1 \tag{1}$$

The primary knock-on dissipates its energy by electronic excitation and by collisions with other atoms in which secondary knock-ons are produced, until eventually it comes to rest as an interstitial. In irradiation with neutrons produced in a nuclear reactor each primary collision produces many secondary knock-ons; this is also true of irradiation with ions of a few keV or more, whereas in the case of irradiation with electrons of 1 MeV or less only one or two vacancies and interstitials are produced by each primary collision. Since the probability of hitting another atom increases as the primary knock-on loses its energy, it travels shorter and shorter distances between producing vacancies. This results in a very high concentration of vacancies near the end of the primary knock-on's path, with the interstitials (secondary knock-ons) moving out of the vicinity and dissipating their energy as heat. The zone of high vacancy concentration and temperature which is produced is called a displacement spike, and it may result in the nucleation of a small void or vacancy type dislocation loop.[27-30]

Although the spatial distribution of lattice defects differs for these three types of irradiation (e.g., displacement spikes are produced only by ions or neutrons and the penetration depth of ions and electrons is quite small), they all result in concentrations of interstitials and vacancies which are well above the thermal equilibrium concentrations. The supersaturation of these lattice defects provides the driving force for the nucleation of voids or dislocation loops, both of which have been observed as a result of irradiation by each of the three irradiations discussed. Since ion irradiation and electron irradiation in a high voltage electron microscope (HVEM) are capable of producing an average defect supersaturation several orders of magnitude greater than that obtainable in nuclear reactors, these methods have been extensively used to investigate the probable effects of long term irradiations in nuclear reactors.

The absorption or emission of point defects by a climbing dislocation requires the presence or nucleation of jogs whose formation is probably more difficult in FCC metals due to the splitting of perfect dislocations. In FCC metals, perfect dislocations with Burgers vectors $b_p = \frac{a}{2}\langle 110\rangle$ are observed to dissociate with a reduction in energy into two Shockley partial dislocations with Burgers vectors $b_s = \frac{a}{6}\langle 112\rangle$ separated by a ribbon of stacking fault whose width depends inversely on the stacking fault energy.[31,32] In order for this configuration (known as an extended dislocation) to climb, the stacking fault must climb in the direction perpendicular to the fault plane. This is expected to occur by the formation and motion of extended jogs, as will be discussed in more detail in section IVC. In general, the formation of jogs is expected to be more difficult on the more widely extended dislocations in metals of lower stacking fault energy. In the present work the effects of stacking fault energy and irradiation damage rate (which controls the supersaturation of point defects) have been studied by observations of the growth rate of prismatic dislocation loops. A perfect, or prismatic, edge dislocation loop is a loop of edge dislocation which may move by glide along a cylinder or prism parallel to its Burgers vector. Prismatic loops formed in FCC metals by quenching or irradiation damage are often observed to be approximately rhombus shaped,[33,34] as in this work. Such loops have sides which lie in the two {111} planes which contain the Burgers vector, and are expected to be dissociated in these planes. Growth or shrinkage of these loops must occur by climb, and the observation in this work that the sides lie accurately in their {111} planes indicates that the jog density must be low, suggesting that the rate of growth is controlled by the rate of jog nucleation rather than by diffusion. In a sufficiently high supersaturation the jog density might become high enough to produce rounded loops whose growth would be diffusion controlled, whereas in low supersaturations the stacking fault energy might be expected to have an effect through its influence on the rate of jog formation.

The growth of dislocation loops in pure FCC metals during irradiation in a high voltage electron microscope (HVEM) has been observed by several authors.[36-39] Both Frank loops (with $b_f = \frac{a}{3}\langle 111\rangle$ Burgers vectors enclosing a stacking fault) and perfect loops have been observed. Especially in the case of the higher stacking fault metals Ni[42,36] and Al[39] the loops tend to have rounded corners indicating high jog densities. Brown,[40] Makin,[41] Norris,[42] and Urban and Wilkens[43] have presented approximate treatments of the problem of diffusion controlled loop growth in thin foils during electron irradiation. Brown[40] and Makin[41] predict that loop size should be proportional to the 1/3 power of time. Norris[42] finds this to be the case only in certain conditions, whereas he predicts a constant growth rate (which fits his observations) when the foil surfaces are the dominant sinks for point defects. Urban and Wilkens[43] obtain a constant growth rate which is a function of capture radii for absorption of interstitials and vacancies by dislocations, and discuss the probable temperature dependance of this growth rate.

The effect of stacking fault energy on dislocation climb has been mentioned by Adda,[44] Brimhall et al.,[45] and Wolfenden[46] as a possible factor in irradiation induced void growth. Wolfenden's observation of void growth[46] in Cu-10% Al (per cent of Al will be given as weight per cent in this paper) is the only example of void formation in low stacking fault energy materials other than stainless steel. Levy et al.[47] failed to observe any voids in Cu-7% Al neutron irradiated under conditions similar to those of Wolfenden.[46] Many factors other than the influence of stacking fault energy on climb are involved in these studies. The present work is an attempt to study more systematically the effect of stacking fault energy in irradiation damage studies.

II. EXPERIMENTAL PROCEDURES

Copper-aluminum alloys with 1.0, 3.5, and 7.5 weight per cent aluminum were prepared from 99.999% pure copper and 99.9999% pure aluminum. Oriented single crystals of these compositions were then grown under vacuum in graphite molds using an induction furnace. These crystals were chemically thinned to .002 to .003 inches thick, and 30 mm diameter discs were spark cut from them. Thin foils were prepared by jet electropolishing these discs with equipment supplied by E. A. Fischione Co.; a solution consisting of one part nitric acid and two parts methanol was used at -40°C with 5-10 volts and 10-20 milliamps.

Irradiation of these foils was carried out using an Hitachi HU 650 electron microscope operated at 650 kV. The damage rate was varied by defocussing the beam with the second condenser lens. A typical growth series was obtained by selecting an area, setting the condenser lens, and then taking micrographs at intervals without changing the condenser lens setting during the photographic exposure; the photographic exposure time was varied to compensate for the different beam current densities used for each irradiation sequence.

The beam current density was then determined by moving the foil out of the field of view, removing the objective aperture, and taking a measurement. Either a lithium detector or a Faraday cup was used to make these measurements. Both the cup and the detector were mounted under the camera and were designed and calibrated by

D. Howitt.[48] In the case of the experiments where the climb rate was determined as a function of damage rate for a given alloy composition, nearly all irradiations were performed in adjacent areas of the same foil by returning to the irradiated area after each measurement of beam current density.

Since the distribution of beam current density with position in the beam is not uniform, this distribution was measured for a few condenser lens settings. This was done by successively moving the beam, taking a reading with the stationary detector, and taking a micrograph to determine the beam position.

Heating of the specimen during irradiation was accomplished with a double tilting hot stage developed for the HU 650 microscope at LBL.[49] In this hot stage the specimen is heated by a small DC resistance heating coil which is double wound to reduce magnetic distortion of the electron beam. The temperature calibration of the stage was accomplished by operating it in a bell jar with a .005 inch thermocouple spot welded to an unthinned specimen disc, and noting the stable temperature resulting from a given power input. The same measured power input was found to reproduce the same stable temperature to within about ±15°C on successive runs. Although it was necessary to allow 15 or 20 minutes for temperature stabilization to occur when the power was turned on, the stage stopped drifting and became quite stable after this, enabling micrographs to be taken without cooling to room temperature.

The growth rates of the loops were measured on contact prints using a magnifier; care was taken to select the same loop on each micrograph by checking its position with respect to stationary features in the foil. Since the loops were rhombic in shape, the separation between both pairs of parallel sides was measured. The growth rate was taken to be the rate of increase in this measurement.

Since it was not possible to nucleate loops at temperatures above about 400°C, growth rates measured at 450°C were obtained using loops initially grown at temperatures below 400°C.

III. OBSERVATIONS

Nucleation and growth of interstitial dislocation loops was observed over a range of temperatures. It was found that there was an upper limit to the temperature range in which loops may be nucleated by the most intense beam available with the HU 650 microscope (about 1.0 amps/cm^2 with the beam focussed). Loops could not be nucleated in a clean foil above about 400°C. At room temperature a very high density of loops (about 10^{14} loops per cm^3) was generally formed, but these never grew to a size which permitted them to be resolved as loops rather than as black dots (Fig. 1). At higher temperatures the number of loops nucleated decreased, and individual loops grew to large enough sizes to enable their shapes to be clearly resolved and their growth rates measured. Loops nucleated below 400°C still grew in moderate beam current densities above this temperature, and it was found that they could be made to grow in the focussed beam up to about 540°C. Above this temperature both nucleation and growth were impossible, but observable shrinkage (with the beam turned off) was not found to occur until about 670°C. Observations of the shrinkage of these loops at high temperatures were complicated by their loss due to slipping out of the foil along their glide cylinders. Although visual observations of loop shrinkage were made, the shrinkage rate was very rapid once shrinkage began, and series of micrographs were not obtained.

A. Nature of the Loops

The loops observed were always perfect type loops with $\frac{a}{2}\langle 110\rangle$

Burgers vectors, and they always had the shape of a rhombus or parallelogram. Figure 2 shows a pure edge perfect dislocation loop whose sides are dissociated and therefore lying exactly in the two {111} planes which contain the Burgers vector. The (110) plane of the loop intersects the $(\bar{1}11)$ and $(1\bar{1}1)$ planes along the $[1\bar{1}2]$ and $[\bar{1}12]$ directions respectively and so the loop sides lie along these directions. By using a stereographic projection corresponding to the exact orientation of a foil as determined from the diffraction pattern, the projections of the rhombus shapes for each of the six possible $\frac{a}{2}\langle 110\rangle$ Burgers vectors may be easily determined. The loop shapes observed were always reasonably close to these idealized shapes. In particular, since in a 110 foil two {111} planes are seen edge on, certain loop sides are observed to lie accurately on these planes as expected. Deviations from the expected orientations of the sides lying in inclined {111} planes are probably due to the loops being rotated somewhat from the pure edge orientation as discussed in section IV A.

Figure 3 shows a set of loops grown at 300°C in a 3.5% Al foil and then cooled to room temperature in order to take stereo micrographs. The Thompson tetrahedron* and projected rhombus loop shapes shown in Fig. 3b are drawn for the foil orientation of Fig. 3a using the Kikuchi diffraction pattern. Since $\vec{g} = \bar{1}11$ in Fig. 3a, $\vec{g}\cdot\vec{b} = 0$ for loops of types A, B, or C. However, since these are edge

*For a discussion of the notation and use of the Thompson tetrahedron, see Hirth and Lothe,[31] page 300.

dislocations, contrast is not completely extinguished in this diffraction condition, and weak images of these loop types are noted on the micrograph. (Due to the orientation of the foil, type B and C loops have almost exactly the same projected shapes; therefore, this shape is simply marked as B on the micrograph.) The shapes of D and E type loops are similar, but type D has a more acute angle than does type E. Note that the D family of loops shows consistently more elongated images than the E family. The F type loops are seen on edge as short, heavy black lines. In Fig. 3c $\vec{g}$ = 002, and only the A type loops (parallel to the foil plane) and the F type loops (perpendicular to the foil plane) show the weak contrast due to the $\vec{g}\cdot\vec{b} = 0$ condition. The $\vec{g}\cdot\vec{b} = 0$ condition does not uniquely determine the Burgers vector of the loops. However, the edge-on view of the F type loops in Fig. 3a shows that their loop plane is {110}, and the fact that $\vec{g}\cdot\vec{b} = 0$ for the A type loops in both Fig. 3a and Fig. 3c shows that $b = \frac{a}{2}\langle 110\rangle$ for these loops. Thus we may postulate that all loops are pure edge perfect loops and test the results of this assumption. First, we see that the $\vec{g}\cdot\vec{b} = 0$ condition for the F type loops in Fig. 3c is consistent with this assumption. Next we observe that the A type loops have sides along <112> directions and so we further postulate that our edge type loops are dissociated in two {111} planes. This assumption leads us to expect the loop shapes of Fig. 3b and allows us to assign tentative Burgers vectors to the loops on the basis of their shapes. Since the observed $\vec{g}\cdot\vec{b} = 0$ conditions fit those predicted by our assumptions, we may conclude that the loops are in fact prismatic loops of the shape shown in Fig. 2.

The images of the loop sides which lie in inclined {111} planes are noticeably wider than those of the sides lying in edge-on {111} planes. This is probably due to the fact that the loop sides are dissociated; for the sides lying in edge-on {111} planes the stacking fault ribbon is seen edge on.

Careful inspection of the images of the A type loops in Fig. 3 reveals that even though these loops must be nearly parallel to the foil surface they are frequently not rhombus shaped but appear as parallelograms. Such deviations from the equilateral shape are not so easily observed in the images of the loops which lie on inclined planes, especially since the shape of these images is affected by the inside-outside contrast phenomenon.

The image of an inclined interstitial or vacancy type dislocation loop may be either inside or outside of the actual position of the dislocation core, depending on the sense of the inclination of the loop relative to the diffraction vector and on whether the loop is of interstitial or vacancy type.[50] In Fig. 3a the images of the D family of loops are more elongated than those of the E family because the D type loops are in inside contrast while the E type loops are in outside contrast. Both are interstitial type, but the inclination of the loop plane is of the opposite sense. Since the tetrahedron is unambiguously oriented by means of the Kikuchi diffraction pattern, we may use the rules of Hirsch et al.[50] to show that the loops are of interstitial type. It is necessary to rely in this case on the fact that the type D loops have a more acute angle than do those of type E, in order to determine sense of the inclination of the loop plane. Figure 4 shows a pair of micrographs of a 111 foil taken with opposite senses of the $2\bar{2}0$ diffraction vector, with the deviation parameter s being positive in both cases. The tetrahedron is again unambiguously oriented using the Kikuchi pattern, and types AD and CD loops, with the opposite senses of inclination with respect to the beam, may be seen to switch from inside to outside contrast in the manner expected of interstitial type loops. Notice that some type AC loops go from outside contrast in Fig. 4a to inside contrast in Fig. 4b, while a few (on the right) exhibit the reverse behavior. This could happen if some were of interstitial type and some of vacancy type, or it could be due to opposite senses of inclination of the loop planes. Since these loops are nearly edge on, and since rotations from the pure edge orientation are present due to internal stresses which may vary with position in the foil (see below), the latter explanation is the more likely one.

Notice that there are virtually no loops of types BC or AB observed here, although they should be in contrast. Since $g \cdot b = 0$ for loops of type DB, they are not observed.

The absence of type AB and type BC loops in Fig. 4 may be due to suppression of their nucleation by the action of internal stresses as suggested by Lewthwaite [7] and Brailsford and Bullough[6] in their discussions of irradiation enhanced creep. Generally, all of the six loop types which were expected to be in contrast were observed, but no really systematic attempt was made to study this question. Micrographs taken with different diffraction vectors and orientations would be necessary to determine whether all six loop types were present in equal numbers in each case. Notice that very few edge-on loops are observed in Fig. 14; this may be another case of suppressed nucleation of one family of loops.

Deviations of about $\pm 5^\circ$ from the pure edge orientation may be observed in the images of the F type loops in Fig. 3, which are seen edge on. Such rotations from the edge orientation may be due to small stresses in the foil and would cause the images of inclined loops to change shape. The sides which are dissociated in {111} planes seen edge on would lie in the same direction in the image since the rotations occur by glide in the {111} planes, but the other sides would deviate from the projected <112> directions for loops which are rotated from the pure edge orientation. The presence of shear stresses which rotate the loops may also cause the sides to bow out on their glide planes. In many cases the loop sides lying in the inclined {111} planes are seen to be rounded, while the sides in the edge-on {111} planes are quite straight. This is what one would expect if the sides were bowed out in their glide planes but not heavily jogged. Figures 3, 10, 14, and 15 show good examples of this sort of image. The sides whose glide planes are seen edge on are generally observed to be quite straight, indicating that they have few jogs. In particular, the A type loops in Fig. 3 have all sides dissociated in edge-on glide planes, and these are all quite straight.

Some loops in Fig. 3 are observed to have irregularities which resemble steps or very large superjogs. Figure 5 shows some series of the growth of loops with such irregularities. Generally these tend to remain on the loops during growth, although sometimes they seem to heal up. They do not move along the loop sides in the regular manner which might be expected if they were superjogs whose passage was responsible for loop growth. They may be due to interactions with nearby small loops, but in most cases no nearby loops are seen to combine with the irregular loops. In a few cases a growing loop develops a group of these steps on one corner as it grows, as in Figs. 5c and 5d. These loops may be approaching the depleted zone near the foil surface. The loop sides seen in edge-on planes may have such irregularities, but aside from these they are quite straight, indicating a low jog density.

B. Growth of the Loops

Figure 6 shows a set of loops which were grown with the beam focussed to its smallest spot. Due to the variation in beam current density across the diameter of the beam, loops nucleate and grow more rapidly in the center of the beam, resulting in larger loops in the center. The measured beam profiles for two different settings of the second condenser lens are shown in Fig. 7. Since at 20,000 times magnification the maximum dimension of the photographic plates used is equivalent to six microns, the variation of the beam current density across the area viewed is fairly small for the more defocussed beam. Nearly all irradiations were done using a measured beam current density less than 0.1 A/cm^2 in order to minimize the effect of the beam profile. The rather uniform loop size distribution in Fig. 3, for instance, was obtained with a beam current density of 0.061 amps/cm^2.

Figures 8a-g show plots of loop size versus time for the growth sequences in Figs. 9-15. There are apparent irregularities in the growth of individual loops; in several cases, for instance, a growing loop seems to be the same size on two successive micrographs. This is certainly due in part to the accuracy of the loop size measurements. Whereas the average increase in size between micrographs is often only 0.2 mm (on a 20,000x micrograph), the width of the dislocation image is about 0.1 mm. However, in some cases loops seem to stop growing for several successive intervals, and in these cases actual cessation of growth must occur.

There are also rather large differences in the average growth rates of different loops in the same irradiation sequence. These differences may be due to different depths of the loops in the foil, different local stresses, or variations of the damage rate with position in the beam.

The growth rate of individual loops does not seem to be a function of their size. Figure 16 shows some plots of size versus time for individual loops which were observed over a large size range. Individual size measurements for these loops are at most 0.2 mm off the straight lines drawn for their growth.

The variation in the growth rate with electron flux was determined at 300°C and at 450°C; the results are plotted in Figs. 17a (300°C) and 17b (450°C). The error bars for the growth rate indicate the maximum and minimum growth rates observed, excluding instances of loops which did not grow at all for long periods. The error bars for Φ are based on estimates of the accuracy of the conversion of the Li detector reading to amps/cm^2 and of the variation in beam current density inherent in a more focussed beam. Notice that in Fig. 17b the growth rate falls to zero below a minimum flux Φ_{min}, which decreases with Al content. This result is not based on extrapolation of the curves; any flux at or below Φ_{min} for a given alloy was observed to give a growth rate less than .008 Å/sec (.001 mm/min as measured on micrographs taken at 20,000x magnification).

Dislocations initially present in the foil were often observed to climb into helices. Good examples of this are found in Figs. 10 and 11. As they grew, the helices exhibited a strong tendency to develop straight segments which lay accurately in {111} planes. Thus, the tendency to remain jog free was present in the helices as well as in the loops. The helices increased their diameters at about the same rate as did the dislocation loops.

IV. DISCUSSION

A. Loop Geometry

The observations indicate that the loops grown were perfect interstitial loops of nearly edge character whose sides were dissociated in {111} planes, resulting in the rhombus or parallelogram shape shown in Fig. 2. A prismatic loop has its least line length at the pure edge orientation, but since the opposite sides interact with each other, the equilibrium orientation is several degrees away from pure edge, and is a function of loop size since the interactions between sides decrease as size increases.

Since opposite sides of such a loop are of opposite sign, shear stresses acting on them cause them to move in opposite directions on their glide planes. This causes the loop to rotate away from its equilibrium orientation, increasing the energy of the loop until the rate of energy increase balances the shear stress and a new equilibrium is reached. Notice that since the loop sides remain in their {111} glide planes the loop does not rotate as a rigid body. A dislocation line which is constrained at its ends bows out with a radius of curvature

$$R = \frac{\mu b_p}{\tau} \, , \qquad (2)$$

where τ is the magnitude of resolved shear stress along the Burgers vector in the glide plane. Therefore, it is to be expected that loops whose sides show a small radius of curvature will be rotated well off their equilibrium (near edge) orientation. The equilibrium orientation of perfect near edge rhombus dislocation loops has been considered by Bullough and Foreman,[51] and their calculations may be extended to determine the equilibrium orientation under any applied stress. Bullough and Foreman's calculation assumes that the loop sides remain straight and lie in their {111} glide planes throughout the rotation. These assumptions will be retained here; it is not expected that the curvature of the sides will alter the elastic energy of the loop appreciably. A more important source of error will be the assumption that the resolved shear stress is equal on all sides of the loop, which would not generally be the real case.

The condition which determines how far the loop will rotate under a given stress is that the energy increment $(dE/d\phi)d\phi$ due to further rotation through a differential angle $d\phi$ must be equal to the increment of work $(dW/d\phi)d\phi$ done by the applied stress. The side length in the pure edge orientation is denoted by L_e, and it increases to

$$L = \frac{L_e}{\cos\phi} \tag{3}$$

during rotation; ϕ is the angle between the side and the pure edge side (Fig. 18). The work increment in rotation of the loop is

$$dW = 4\tau b_p dA \quad , \tag{4}$$

where dA is the differential area swept out by the side and the factor of four is due to there being four sides. Since

$$dA = \frac{L^2 d\phi}{2} \quad , \tag{5}$$

$$\frac{dW}{d\phi} = \frac{2L_e^{\,2}\tau b_p}{\cos^2\phi} \quad , \tag{6}$$

and since

$$\frac{dE}{d\phi} = \frac{dW}{d\phi} \quad , \tag{7}$$

$$\tau = \frac{\cos^2\phi}{2L_e^{\,2} b_p} \cdot \frac{dE}{d\phi} \tag{8}$$

Bullough and Foreman[51] considered rotations about the <100> major axis and the <110> minor axis of a rhombus shaped prismatic loop and showed that the energy minimum was deeper for rotation about the major axis. Their calculations use an expression for the total elastic energy of the loop which is plotted for different loop sizes in Cu in Fig. 19a; Fig. 19b shows the equilibrium orientation of the loop as a function of stress for different size loops. These are calculated on the assumption that the resolved shear stress is equal on all sides and that the rotation is about the <100> major axis. The results for the minor axis (Figs. 19c and 19d) are quite similar, except that there is no minimum in the energy. The minimum appears only for smaller loops.

A loop whose pure edge orientation is inclined to the foil, and which has sides which lie in inclined {111} planes, will show curvature of its sides if stresses are present which bow the sides out on their glide planes. Consider a foil which is viewed exactly along the [110] direction. The inclined loops may rotate by glide in such a manner as to produce a more nearly rectangular shape or a more acute shape. Depending on whether the rotation of the loop is about the major or the minor axis (or some general axis), the more rectangular shape may produce an image in which the sides appear either curved outwards (convex) or curved inwards (concave). Examples of loops with convex and concave images are shown in Fig. 20. Figure 21 shows the projected shapes of an inclined loop viewed exactly along a <110> direction for different values of the angle ϕ. The sides are drawn straight because they may in fact be either convex or concave. Comparison of individual images with these shapes gives an approximate measurement of the deviation from the pure edge orientation of individual loops. The observed radius of curvature of the loop sides may be compared with the radius of curvature which is calculated to be necessary to maintain the observed loop orientation. Similarly the measured radius of curvature may be used to determine the expected rotation which may then be compared with the observed rotation. A number of such comparisons are listed in Table I. The calculated values given are for rotation about the <100> major axis.

The measurement of the angle ϕ by comparison with the shapes drawn in Fig. 21 is complicated by the change of shape which accompanies small changes in the viewing direction (as in Fig. 3) and by the curvature of the sides. The measured values of ϕ are therefore probably only accurate to about $\pm 5°$. Measurements of the radius of curvature of the loop sides are complicated by the inclination of the loop plane to the viewing direction and by effects of image contrast. Since the image of a dislocation does not lie exactly at the dislocation core, the radius of curvature of the dislocation line may not be accurately represented by its image.

The measured radii of curvature in Table I are all considerably

Table I. Measured anc Calculated Radii of Curvature for Rotation about the <100> Major Axis

Loop #	$L_e(\mu)$	R (μ)		φ (degrees)	
		Meas.	Calc.	Meas.	Calc.
1	0.2	0.4	17.9*	5	>30
2	0.2	0.4	17.9*	5	>30
3	0.15	0.3-0.4	11.4-19.1	8-10	>30
4	0.15	0.3-0.4	11.4-19.1	8-10	>30
5	0.15	0.3-0.4	11.4-19.1	8-10	>30
6	0.15	0.3-0.4	11.4-19.1	8-10	>30
7	0.15	0.3-0.4	11.4-19.1	8-10	>30
8	0.3	0.5 or more	2.8	20	>30
9	0.1	0.5	6.2	15	28
10	0.3	0.3-0.4	1.0 or less	30-35	>30
11	0.1	0.5 or more	7.2	10	28 or less

*These orientations are unstable -- the loop should rotate to the other side of the edge orientation.

smaller than those calculated from the observed loop orientations. This means that the stresses which are necessary to produce the observed radii of curvature should rotate the loops much farther from the edge orientation than they do. Apparently the loops resist rotation, possibly due to the presence of a Cottrell atmosphere or to some resistance of the loop corners to glide.

Although the observed and calculated loop rotations do not agree, the curvature of the loop sides must be due to glide. Curvature due to climb would be visible in the images of loop sides lying in edge-on {111} planes. However, this observation is complicated somewhat by the fact that we do not in general see these planes exactly edge on. It is desirable to have a separate proof that loop sides whose images are curved are bowed out in their glide planes rather than by climb. The loop marked A in Fig. 22 is seen to disappear by slipping to the foil surface, leaving behind a short segment of dislocation and a faint image resembling a shadow, where the rest of the loop intersected the surface. The shadow image has the shape of the intersection of the glide prism with the foil surface. Before slipping out of the foil, the loop is seen to have had a pronounced curvature of its sides, but the sides of the shadow image are quite straight, indicating that the curvature of the sides was due to glide rather than climb.

The zero stress equilibrium orientation of a loop is farther away from pure edge for a smaller loop, and it takes more stress to rotate a smaller loop from this orientation. A given stress will therefore produce different orientations for different loop sizes, and a loop which grows under constant stress should change its orientation as it grows. Figure 22 shows a series of micrographs of a loop which rotates slowly as it grows under the influence of an approximately constant stress (as indicated by the curvature of its sides).

Perfect dislocations in FCC metals of low stacking fault energy are generally observed to be dissociated into a pair of Shockley partial dislocations separated by a ribbon of stacking fault. The sides of the prismatic loops in this work are segments of perfect dislocations which are expected to be dissociated in the {111} planes in which they lie, as illustrated in Fig. 2. The dislocations at the loop corners are stair rod dislocations, which are required to conserve the Burgers vector at the junction between the Shockley partials on the two {111} planes. It is assumed that all the stacking faults are intrinsic; if the order of the Shockley partials were reversed on any side, an extrinsic fault and a different stair rod dipole at either end would result. It is generally considered most likely that perfect dislocations split in such a manner as to produce intrinsic stacking faults, and this assumption will be made in this discussion. The possibility of the presence of some extrinsic faults should not greatly affect any arguments presented herein. The line tension of the stair rods at the loop corners probably pulls the Shockley partials together slightly at the corners, producing the partial constriction illustrated in Fig. 2.

The equilibrium width d of the stacking fault ribbon on an extended dislocation in an FCC metal of stacking fault energy γ is given[31] by

$$d = \frac{\mu b_s^{\,2}}{8\pi\gamma} \cdot \frac{(2-\nu)}{(1-\nu)} \left(1 - \frac{2\nu\cos 2\beta}{2-\nu}\right) , \qquad (9)$$

where μ is the shear modulus, b_s is the magnitude of the Shockley Burgers vector, and β is the angle between the perfect a/2<110> Burgers vector and the dislocation line. Notice that for a prismatic loop which has rotated away from the edge orientation under the action of a shear stress, the stacking fault width is decreased by the deviation from pure edge character. For a dislocation about 20° from pure edge under no stress, d is only about six tenths of the value for a pure edge dislocation.

The presence of stresses in the foil will in general affect the spacing between the Shockley partials (Hirth and Lothe,[31] page 330). Whether this spacing is increased or decreased depends on the direction of the resolved shear stress on the slip plane. The component of resolved shear stress acting perpendicular to the perfect Burgers vector either increases or decreases d depending on its sense. The component acting parallel to the perfect Burgers vector must tend to decrease d in a constrained dislocation such as a loop. The maximum effect of stress is to add or subtract a term of the order of τb_s (where τ is the resolved shear stress) to the stacking fault energy γ in Equation 9. Since the maximum observed shear stresses were of the order of 10^8 dynes/cm^2, τb_s is of the order of 2 ergs/cm^2. Thus in the 1% Al alloy d should be only slightly affected by stress, whereas the spacing in the 7.5% Al alloy might be strongly affected by stress. In the absence of stress, the values of d for a pure edge dislocation in the alloys used in this work are 54.2 Å for 1% Al (γ = 30 ergs/cm^2); 163 Å for 3.5% Al (γ = 10 ergs/cm^2); and 813 Å for 7.5% Al (γ = 2 ergs/cm^2). These values of γ were obtained from Howie and Swann.[52] Recent weak beam measurements of the stacking fault energies of these alloys by Cockayne[14] give slightly different values: γ = 5, 15, and 30 ergs/cm^2 for the 7.5%, 3.5%, and 1% Al alloys. The value of γ is known to increase somewhat with temperature,[35] and this would result in a change in d with temperature.

B. Distribution of Point Defects in Thin Foils During Irradiation

The diffusion of interstitials and vacancies to the foil surfaces during irradiation produces a variation in the point defect concentrations with depth in the foil. Quantitative analysis of the rates of growth of dislocation loops due to clustering of point defects thus requires knowledge of the distribution of the defects in the foil. The usual approach to this problem is to say that there exist denuded zones near the foil surfaces in which the point defect concentrations are too low to cause growth of dislocation loops or voids, while in the center part of the foil conditions are assumed to be uniform.[21,41]

Foreman[53] has considered the problem of simultaneous production, recombination, and diffusion to the surfaces of vacancies and interstitials during irradiation of thin foils. The steady state is reached when the rate of loss of point defects from a slab of material parallel to the foil surface is equal to their rate of production R. The rate of loss consists of the recombination rate plus the net rate at which the defects diffuse out of the slab, given by Fick's second law of diffusion. Also, in the steady state interstitials and vacancies must be lost at the surface at equal rates, which means that the interstitial and vacancy concentrations C_i and C_v are related by

$$C_i D_i = C_v D_v \quad , \tag{10}$$

where D_i and D_v are the interstitial and vacancy diffusion coefficients,

$$D_i = \lambda^2 \gamma_i \nu_i$$
$$D_v = \lambda^2 \gamma_v \nu_v \quad , \tag{11}$$

where λ is the interatomic jump distance, γ_i and γ_v are geometrical constants which are both nearly unity,[53] and

$$\nu_i = \nu_0 \exp(-E_{mi}/kT)$$
$$\nu_v = \nu_0 \exp(-E_{mv}/kT) \quad , \tag{12}$$

where E_{mi} and E_{mv} are the migration energies for interstitials and vacancies and ν_0 is the vibration frequency of the atom in the direction of the saddle point. The vacancy concentration profiles are given in Fig. 23, where C_v/C_v^∞ is plotted as a function of the normalized depth in the foil for different values of the parameter f:

$$f = \frac{Rt^4\delta}{\nu_v\gamma_i\gamma_v\lambda^4} \quad , \tag{13}$$

where δ is the coordination number for interstitial-vacancy recombination ($\delta \approx 10$), t is the foil thickness, and R is the point defect production rate in displacements per atom per second (dpa/sec). C_v^∞ is the recombination limited vacancy concentration in bulk material, given by

$$C_v^\infty = \left(\frac{R\gamma_i}{\nu_v\gamma_v\delta}\right)^{\frac{1}{2}} \tag{14}$$

The value of R is determined simply from

$$R = \Phi\sigma \quad , \tag{15}$$

where Φ is the beam current density in electrons/cm^2sec, and σ is the displacement cross section for 650 kV electrons; at this energy σ is about 25 barns (one barn = $10^{-24}cm^2$) for both Cu and Al.[54] Thus if the beam current is given in amps/cm^2,

$$R = 1.56 \times 10^{-4}\Phi \text{ dpa/sec} \tag{16}$$

The partial molar free energies of vacancies and interstitials, $\overline{G}_v$ and $\overline{G}_i$, are important in determining the nucleation rate of dislocation loops or jogs. They are given by

$$\overline{G}_v = kT \ln(C_v/C_v^0)$$

$$\overline{G}_i = kT \ln(C_i/C_i^0) \quad , \tag{17}$$

where C_v^0 and C_i^0 are the equilibrium vacancy and interstitial concentrations,

$$C_v^0 = \exp(S_{fv}/k - E_{fv}/kT)$$

$$C_i^0 = \exp(S_{fi}/k - E_{fi}/kT) \tag{18}$$

Values of f, C_v^∞, $\overline{G}_v^\infty$, and $\overline{G}_i^\infty$ are given for 300°C in Table II and for 450°C in Table III for different foil thicknesses and damage rates. The superscript ∞ refers to the value for bulk material or very thick foils; C_i^∞ is related to C_v^∞ by Equation 10. These values refer to the maximum concentrations in the center of a thick foil. The beam current densities used in this work varied from .001 to 1.0 amps/cm^2 (1.56×10^{-7} to 1.56×10^{-4} dpa/sec), and the foil thicknesses were generally 0.4 to 0.5 microns. The values used for the various parameters are as follows:

$\delta = 10$

$\lambda = 2.56$ Å

$\gamma_i = \gamma_v = 1$

$\nu_0 = 10^{13}\text{sec}^{-1}$

$E_{mi} = .05$ eV

$E_{mv} = 1.16$ eV

$E_{fi} = 4.0$ eV

$E_{fv} = 1.17$ eV

$S_{fi} = 0.8$ k

$S_{fv} = 1.5$ k

$k = 8.617 \times 10^{-5}$ eV/cm^3 (Boltzmann's constant)

The value of ν_0, the vibrational frequency of an atom in the lattice, was assumed to be the same for interstitials as for atoms in normal lattice positions. The choice of ν_0 was made from several sources.[55,56,57] Foreman's use of $\nu_0 = 10^{15}\text{sec}^{-1}$ seems unjustified. The values used for the migration energies, formation energies, and formation entropies were obtained from Cahn.[55] The value of E_{fi} has a marked effect on the calculated value of $\overline{G}_1^{\infty}$, and it should be noted that theoretical values for E_{fi} range from about 2 to 6 eV.[55] The values of the other energies are more generally agreed upon.

The partial molar free energies and the vecancy and interstitial concentrations given in Tables II and III represent the maximum values possible for the given conditions in a thin foil. If the parameter f is greater than about 10^4, these values are attained at the center of the foil (see Fig. 23), but for $f < 10^4$ the maximum concentrations and $\overline{G}$ values are less than those in the tables. For large values of f the diffusion profiles in Fig. 23 have a flat region in the center of the foil and a rapidly decreasing point defect concentration as the surfaces are approached. This type of profile suggests the denuded zones mentioned earlier, whereas the profiles for values of f less than

Table II. Point Defect Distribution Parameters at 300°C*

t	R	f	C_v^{∞}	$\overline{G_i^{\infty}}$ (eV)	$\overline{G_v^{\infty}}$ (eV)
.40	10^{-3}	9.6×10^{7}	4.00×10^{-4}	2.46	0.71
.45	"	1.5×10^{8}	"	"	"
.50	"	2.3×10^{8}	"	"	"
.55	"	3.4×10^{8}	"	"	"
.40	10^{-4}	9.6×10^{6}	1.26×10^{-4}	2.41	0.65
.45	"	1.5×10^{7}	"	"	"
.50	"	2.3×10^{7}	"	"	"
.55	"	3.4×10^{7}	"	"	"
.40	10^{-5}	9.6×10^{6}	4.00×10^{-5}	2.35	0.60
.45	"	1.5×10^{5}	"	"	"
.50	"	2.3×10^{5}	"	"	"
.55	"	3.4×10^{5}	"	"	"
.40	10^{-6}	9.6×10^{5}	1.26×10^{-5}	2.29	0.54
.45	"	1.5×10^{4}	"	"	"
.50	"	2.3×10^{4}	"	"	"
.55	"	3.4×10^{4}	"	"	"
.40	10^{-7}	9.6×10^{4}	4.00×10^{-6}	2.24	0.48
.45	"	1.5×10^{3}	"	"	"
.50	"	2.3×10^{3}	"	"	"
.55	"	3.4×10^{3}	"	"	"

*t is given in microns, and R in dpa/sec.

Table III. Point Defect Distribution Parameters at 450°C*

t	R	f	C_v^∞	$\overline{G_i^\infty}$ (eV)	$\overline{G_v^\infty}$ (eV)
.40	10^{-3}	1.17×10^6	3.50×10^{-5}	2.20	0.44
.45	"	1.79×10^6	"	"	"
.50	"	2.62×10^6	"	"	"
.55	"	3.70×10^6	"	"	"
.40	10^{-4}	1.17×10^5	1.10×10^{-5}	2.13	0.37
.45	"	1.79×10^5	"	"	"
.50	"	2.62×10^5	"	"	"
.55	"	3.70×10^5	"	"	"
.40	10^{-5}	1.17×10^4	3.50×10^{-6}	2.06	0.29
.45	"	1.79×10^4	"	"	"
.50	"	2.62×10^4	"	"	"
.55	"	3.70×10^4	"	"	"
.40	10^{-6}	1.17×10^3	1.10×10^{-6}	1.99	0.22
.45	"	1.79×10^3	"	"	"
.50	"	2.62×10^3	"	"	"
.55	"	3.70×10^3	"	"	"
.40	10^{-7}	1.17×10^2	3.50×10^{-7}	1.91	0.15
.45	"	1.79×10^2	"	"	"
.50	"	2.62×10^2	"	"	"
.55	"	3.70×10^2	"	"	"

*t is given in microns, and R in dpa/sec.

about 10^4 exhibit a more gradual variation of concentration with depth in the foil. Notice that while f increases linearly with R, it is proportional to the fourth power of the foil thickness t, and it decreases exponentially with temperature. Thus good diffusion profiles are obtained in thick foils at low temperatures and with high damage rates.

The presence of dislocation loops in the foil will have some effect on the diffusion profiles in Fig. 23. According to Foreman,[53] the dislocations may be approximately treated as a continuum non-preferential sink by adding a term $\rho D_v C_v$ to the recombination rate before solving the diffusion equation (ρ here is the dislocation density). In fact the dislocations are preferential sinks for interstitials, but the interstitial bias is small enough that it may be ignored for this purpose. Foreman showed that a dislocation density of $4 \times 10^{10}/cm^2$ in a ½ micron thick foil has the effect of markedly improving the diffusion profiles in Fig. 23 so that even for f = 1 the profile is better than for f = 10^3 without the dislocation sinks. However, this is a rather high dislocation density, and in this work the loops constitute a dislocation density of only about $4 \times 10^8/cm^2$ so that the diffusion profiles of Fig. 23 are not appreciably affected.

It is instructive to consider briefly what becomes of the point defects after they are produced. The diffusive flux of defects to the surface is easily computed from the concentration gradient at the surface, which was determined during the solution of the diffusion problem. For a foil 0.5 microns thick, a beam current of 0.02

amps/cm^2, and a temperature of 450°C, there are 1.32×10^{13} defects/sec produced per square centimeter of foil, of which 3.64×10^{12} defects/cm^{2}sec or 27.6% leave the two foil surfaces. Under these conditions the maximum growth rate measured was about 1.6×10^{-8} cm/sec for a loop density of about 10^9 per square centimeter of foil with an average side length of 0.1 micron. A simple calculation shows that this corresponds to the absorption of 6.4×10^{11} interstitials/cm^{2}sec, which is about 5% of the defect production rate. Thus, 5% of the interstitials produced are absorbed by climb of the dislocation loops, 27.6% are lost at the surface, and the rest recombine with vacancies. At lower temperatures the fraction of the defects lost at the surface is smaller, all other conditions being equal.

C. Jog Formation on Extended Dislocations

A unit jog on an undissociated edge dislocation is simply a step in the extra half plane of atoms above the slip plane; the dislocation on one side of the jog lies in a slip plane one interplanar distance higher than on the other side of the jog. A row of interstitials added to the edge of the half plane produces a pair of jogs of opposite sign, as does the addition or emission of a row of vacancies. The emission of interstitials from a dislocation is essentially impossible because of the high energy of formation of interstitials. Jogs of the same sign may combine to form superjogs of height greater than one interplanar spacing.

Consider a pair of opposite sign superjogs on an undissociated perfect edge dislocation in an FCC metal. If this dislocation dissociates, the superjogs will also tend to dissociate,[31] forming the extended superjog pair shown in Fig. 24a. It is assumed that the dislocation segments not on the original glide plane are dissociated on the other {111} plane containing the Burgers vector; all faults are intrinsic. The acute jog has a stair rod dipole with opposite Burgers vectors $\gamma\delta$ and $\delta\gamma$ of the type a/6<110>, and the obtuse jog has a stair rod dipole with opposite Burgers vectors $AB/\delta\gamma$ and $\delta\gamma/AB$ of the type a/3<100>. The line tension of these stair rod dislocations probably pulls the Shockley partial dislocations together somewhat at the jogs, producing a partial constriction. In the case of jogs of unit height (also called jog lines), the strain fields of the stair rods must almost completely cancel each other since the stair rods are of opposite sign and only one interplanar distance apart. Their line tension is then only due to the energy of the dislocation core given by Friedel[32] as approximately

$$E_{core} = \frac{\zeta\mu b^2}{4\pi} \qquad (19)$$

with ζ about one or two. Friedel estimates the energy per unit length of a closely spaced stair rod dipole as about $\mu b_p^2/25$, where b_p is the magnitude of the perfect a/2<110> Burgers vector and $\mu = 5.46 \times 10^{11}$ dynes/cm^2 is the shear modulus for Cu. Equation 19 with $\zeta = 1.5$ gives the line tension of a stair rod dipole as about $\mu b_p^2/19$ for a/3<100> stair rods or $\mu b_p^2/38$ for a/6<110> stair rods. Estimates of the line energy of the a/6<110> dipole vary from $\mu b_p^2/45$ to $\mu b_p^2/12$ according to Kuhlmann-Wilsdorf.[58]

The representation of a jog line as a dipole separated by a stacking fault is questionable since the stacking fault is really within the dislocation core region. However, it is conceivable that there is some effect of stacking fault energy on the core energy of such a configuration.

The mechanism of formation of jogs on a dislocation which is already extended is not well known. Several models have been suggested.[59,61-64] The simplest model[59] requires the formation of a constriction in the dislocation by pinching together the Shockley partials to form a segment of perfect dislocation which may then climb by the formation of a jog pair (Fig. 24b). The energy of such a constriction consists of the work done in forcing the Shockley partials together, and is approximately[59,32]

$$W_c = \frac{\mu b_p^{\,2} d}{30} \left(\ln \frac{d}{b_p}\right)^{\frac{1}{2}} , \tag{20}$$

where d is the equilibrium width of the stacking fault given by Equation 9. Since one constriction is required on each side of the jog, the energy necessary for jog formation is $2W_c$; the values of $2W_c$ are 14.1, 49.2, and 289.7 eV for pure edge dislocations in the 1%, 3.5%, and 7.5% Al alloys in the absence of stress.

The existence of constrictions on widely extended dislocations in Cu-Si and Cu-Al alloys has been experimentally observed by Carter and Ray[60] by the use of weak-beam dark field electron microscopy. However, these constrictions were observed in material which had been deformed by bending before preparation of thin foils, and were probably formed by dislocation interactions during deformation.

The energy of an extended jog pair is the sum of the energies of the stair rods, the extra lengths of Shockley partials, and the extra area of stacking fault. The Shockley jogs may be assumed to have only the energy associated with their cores, given by Equation 19, because they are very short and their strain fields are lost in those of the dipoles (see Friedel,[32] page 172, and Hirth and Lothe,[31] pages 230 and 247). This is especially true if the two jog lines are close together since then the Shockley strain fields cancel each other. The energy associated with the extra stacking fault may be neglected since for $\gamma = 10$ ergs/cm^2 it amounts to only .004 eV per atom length of jog line. Using Equation 19 for the energy of the stair rods (with $\zeta = 1.5$), and denoting the magnitudes of the a/6<110>, a/3<100>, and a/6<112> Burgers vectors as $b_{\gamma\delta}$, $b_{AB/\delta\gamma}$, and b_s respectively, the energy W_{jp} of the extended unit jog pair is given by

$$W_{jp} = \frac{3\mu d}{8\pi}\left(2b_{\gamma\delta}^{2} + 2b_{AB/\delta\gamma}^{2}\right) + \frac{3\mu d_{111} b_s^{2}}{8\pi} , \qquad (21)$$

where $d_{111} = 2.09$ Å is the spacing of {111} planes. This may be a slight overestimate because there is probably a small decrease in energy associated with a partial constriction of the dislocation, but the difference is certainly no larger than the other uncertainties involved. The values of W_{jp} for a pure edge dislocation under no stress are 11.9, 35.1, and 174.6 eV for the 1%, 3.5%, and 7.5% Al alloys respectively. The values of W_{jp} and $2W_c$ are both much greater than $\overline{G}_1$ in the present experiment (about 2 eV from Tables II and III).

Since $\overline{G}_i$ is much less than either W_{jp} or $2W_c$, an interstitial cannot form a jog pair without thermal activation. However, the difference between $\overline{G}_i$ and these formation energies is so large that the rate of thermal jog formation in this supersaturation should be negligible unless some mechanism operates in which several interstitials participate. For instance, if the interaction energy W_{int} between two jogs formed on an initially straight dislocation is taken into consideration, the total energy of formation of a pair of jogs separated by a distance D is given by

$$\Delta G = W_f + W_{int} - \frac{D}{\ell}\,\overline{G}_i \ , \qquad (22)$$

where W_f is the elastic energy of a pair of jogs (e.g., W_{jp} or $2W_c$), and $\ell = \sqrt{6}\ a/4$ is the jog spacing per interstitial. For undissociated jogs W_{int} is given by

$$W_{int} = -\frac{K_{int}}{D} \qquad (23)$$

according to Hirthe and Lothe[31] (page 247), where K_{int} is a positive constant; this expression would be somewhat different for extended jogs, but the general form would be the same at larger separations. If we differentiate ΔG with respect to D and set the result equal to zero, we can find D*, the critical separation beyond which the jogs separate spontaneously by absorption of interstitials. D* then gives ΔG^*, the activation energy for jog pair formation;

$$D^* = \left(\frac{K_{int}\ell}{\overline{G}_i}\right)^{1/2} \qquad (24)$$

$$\Delta G^* = W_f - \frac{K_{int}}{D^*} - \frac{\bar{G}_i D^*}{\ell} \qquad (25)$$

The activation energies found using this model are still of the same order as W_{jp} or $2W_c$ and would yield negligible jog nucleation rates.

A number of alternate models for the nucleation of jog pairs on extended dislocations have been suggested.[61-64] In most of these models the questions of the activation energy for nucleation of a stable jog pair and the possible effect of stacking fault energy have not been discussed. Two of the more interesting models are illustrated in Figs. 25 and 26. The triangular step on the stacking fault ribbon in Fig. 25a was suggested by Thomson and Balluffi,[63] and a similar configuration was discussed by Escaig,[64] and by Friedel,[32] page 172. Thomson and Balluffi referred to the dipoles which extend into the fault as stair rod dipoles, whereas Escaig considered them to be Shockley dipoles. In the case of stair rod dipoles, illustrated in Fig. 25b, each additional interstitial (or vacancy) produces the same small increase in the length of the stair rod dipoles. This is easily seen if the dipole $\delta\beta$-$\beta\delta$ is imagined to move one row to the left with the absorption or emission of each point defect. The associated increase in energy is only about 0.2 eV, and the absorption of an interstitial with $\bar{G}_i \approx 2$ eV is therefore accompanied by a considerable decrease in the free energy of the crystal. The first point defect must produce the three short jogs $A\beta$, $\gamma\beta$, and $A\gamma$ in addition to the constant increase in the stair rod dipole length. The core energy of these jogs is about 0.3 eV, so for supersaturations such that $\bar{G}$ is larger than about 0.5 eV the growth of this type of triangular step need not be thermally activated. The configuration would grow with a continuous decrease in the free energy of the crystal until it reached the other side of the extended dislocation and formed a double jogline as in Fig. 25c. This model suggests that the splitting width of extended dislocations should not affect the rate of jog formation (except for the possible difference in dipole core energy in crystals of different stacking fault energy, which would only affect the critical supersaturation below which jog formation becomes thermally activated). It should be noted here that the description of the atomic disorder associated with the addition of one point defect to the edge of the fault as an array of dislocations is very approximate. However, it may give results of the correct order of magnitude and will be used in the absence of more detailed calculations of the energy of such a configuration.

The results of the present work indicate that jog formation on extended dislocations is a thermally activated process even for $\overline{G}_i \simeq 2$ eV (in this range of γ) and that the activation energy for the process is a function of the stacking fault energy.

In the case of Escaig's model for the triangular step,[32,64] the above arguments still hold except that the dipole energy is somewhat increased since the Shockley Burgers vector is of greater magnitude than that of the stair rod.

Thomson and Balluffi,[63] Escaig,[64] and Friedel[32] (pages 169-173) also note that the formation of a Frank loop in the ribbon of intrinsic stacking fault can eliminate the fault on the interior of the loop. This loop may grow out to the edge of the fault and combine with the Shockley partials to form a perfect dislocation at either edge. The perfect dislocations formed do not lie in either of their slip planes, and it is difficult to see how the resulting configuration could form a jog pair. As discussed by Friedel and Escaig, this process requires activation energies of the same order as those for the triangular steps already discussed. It would not be expected to be thermally activated in the present experiment, and should be only slightly affected by the stacking fault energy.

Thomson and Balluffi[63] suggested that a row of point defects along one of the Shockley partials of an extended dislocation may be thought of as a small prismatic dislocation loop which may dissociate to form an extended jog pair. This has also been discussed by Hirth and Lothe[31] (pages 531-533); the model is illustrated in Fig. 26.

While such a model seems reasonable for the absorption of a row of point defects, it seems unlikely that the configuration of Fig. 26c will dissociate by glide to form a complete jog pair as suggested by Hirth and Lothe and Thomson and Balluffi. While the Shockley partials γA and $B\gamma$ at the top of the step will tend to repel each other, it must be realized that the γA Shockley is one member of a dipole whose net interaction with the $B\gamma$ Shockley must be very nearly zero when the dipole is closely spaced. The short Shockley jogs $B\delta$ and δA would not interact nearly as strongly as like segments of long dislocations, and probably provide insufficient force to extend the configuration across the fault against the line tension of the stair rod dipoles. Also note that when the separation between the jogs is small the attraction of δB to Bδ will nearly balance the repulsive force of δA.

These arguments are no longer valid when the height and separation of the jog pair become large enough because then the stress fields of the Shockley partials on the same side of the loop no longer overlap completely. Thus at some critical size the loop will dissociate to form an extended jog pair.

Now consider for a moment a small prismatic loop in the bulk material as in Fig. 2. When this loop is very small, the repulsive interactions between the Shockley partials on opposite sides of the fault are partially cancelled by the attraction of the Shockley partials on the other side of the loop. Thus small loops should not be extended to the same distance d as large loops or long straight dislocations. The value of d as a function of loop size may be computed from the force of interaction of two coaxial prismatic loops of the same size. For circular loops Grilhe and Seshan[65] conclude that the splitting d becomes about that of long straight dislocations when the loop diameter is of the same order as the equilibrium value of d.

Grilhe[66] suggests that we may distinguish two cases. Let r_1 be the radius above which a small loop formed adjacent to an extended dislocation spontaneously dissociates to form an extended jog pair, and let r_2 be the critical radius for nucleation of loops. The critical radius r_2 will be smaller near the dislocation because the strain field of the existing dislocation may aid in the nucleation process. r_2 is also a function of the supersaturation. In the first case, when r_2 near the dislocation is less than r_1, the rate controlling step for climb (i.e., for jog nucleation) is the formation of the loop. In the second case, when $r_2 > r_1$, jogs are nucleated directly.

The stacking fault energy clearly affects r_1. The effect of stacking fault energy on r_2 for loops near an extended dislocation would be due to the change in the strength of the strain field of the Shockley partial at the opposite side of the stacking fault ribbon with the fault width. Both Shockley partials have some edge component which favors the presence of interstitials on the tension side of the half plane, and therefore reduces r_2. This effect would be greater for small values of d, so for alloys of high stacking fault energy the value of r_2 should be smaller. Thus for the case $r_2 < r_1$, the stacking fault energy would affect the jog nucleation rate through its effect on r_2. For the case $r_1 > r_2$, the jog nucleation rate would be affected by the influence of stacking fault energy on r_1. These arguments are equally valid for the double jog model of Fig. 26, and for the case of small loops nucleated near a dislocation but not at first combined with it. However, it seems likely that small loops which are very close to a dislocation will combine with it in the early stages of their growth due to the attraction of the opposite sign Shockley partials of the loop and the extended dislocation.

This model is in qualitative agreement with the observations of the present work in that it provides a stacking fault energy dependent activation energy for jog nucleation. This activation energy is probably low because it involves the participation of several point defects in the formation of the critical sized nucleus. However, the model is not yet developed sufficiently to make quantitative predictions of the values r_1 and r_2 and the energies associated with them. It is important to realize that the classical treatment of the nucleation of dislocation loops by condensation of point defects is unable to quantitatively explain the observed loop densities in quenched metals (see Hirth and Lothe,[31] pages 560-564, for a discussion of this point). This is probably either due to the overestimation of the energy of very small dislocation loops by the use of expressions valid for larger loops, or due to heterogeneous nucleation. In any case the present understanding of the nucleation of small loops is not complete, and it is therefore unlikely that the above arguments concerning the nucleation of loops near dislocations will be made quantitatively satisfactory in the near future. The approximate dependence of r_1 and r_2 on stacking fault energy may, however, be determined.

Once formed, jogs may move along a dislocation by absorption of whichever type of point defect formed them. The process by which this absorption takes place on extended jogs or superjogs is not well understood but should have a lower activation energy than that for jog formation unless it is necessary to form a constriction before absorption or emission can take place. In the case of a jog line, the absorption of a point defect does not result in any change in the jog configuration except that it is moved over one step. However, the addition of one point defect to an extended superjog would involve the creation of extra lengths of stair rod, and this may have to proceed by some mechanism similar to those discussed above for jog nucleation. However, in a supersaturation such that jog nucleation is slow, one would expect any barrier to jog motion to be less important than that for jog nucleation.

D. The Rate of Jog Nucleation

The rate of nucleation of jogs on a dislocation loop may be expressed[31] as

$$J = Z\omega n_c \quad , \tag{26}$$

where n_c is the number of nuclei of critical size on the loop; ω is the frequency with which the critical nuclei absorb another interstitial, thereby becoming stable with respect to further growth. Z is the Zeldovich factor, which takes into account the fact that nuclei of the critical size plus one point defect may shrink by thermal activation if their energy is not sufficiently smaller than that of the critical size nucleus. Z is given by Feder et al.[67] as

$$Z = \left[\frac{-(\partial^2 \Delta G/\partial i^2)_{i=i^*}}{2\pi kT}\right]^{\frac{1}{2}} \quad , \tag{27}$$

where ΔG is the change in free energy of the crystal due to formation of the nucleus, i is the number of point defects in the nucleus, and i* is the number of point defects in the critical size nucleus. The value of Z for loop nucleation is about 0.1,[31] and we may use this value in the absence of a detailed nucleation model. ω is given by

$$\omega = C_i' N \nu_i \quad , \tag{28}$$

where C_i' is the interstitial concentration at the loop, ν_i is the interstitial jump frequency, and N is the number of interstitial sites adjacent to the critical size nucleus. Notice that N is a function of the critical size. One should also take into account the possibility of diffusion of interstitials along the dislocation to the critical nucleus. The concentration of critical nuclei n_c is just

$$n_c = n_s e^{-\Delta G^*/kT} \quad , \tag{29}$$

where ΔG^* is the activation energy and n_s is the number of nucleation sites on the loop,

$$n_s \propto \frac{L}{\ell} \quad , \tag{30}$$

where L is the length of the loop sides, and $\ell = \sqrt{6}\, a/4$ as before.

Since the loops in this work are observed to remain rhombus shaped and straight sided throughout growth, they must have low jog densities, or at least they must have approximately equal numbers of opposite sign jogs. The average spacing between jogs should be controlled by the relative rates of jog nucleation and jog motion. Since we have observed that the loop growth rate falls to effectively zero for damage rates which should still yield appreciable supersaturations of point defects, it is reasonable to postulate that the growth rate is determined by the rate of jog nucleation, rather than by the rate of diffusion. If the rate of jog motion were very large compared to the jog nucleation rate, jogs would move along a loop side to the loop corners before new jogs were nucleated. In this extreme case, each jog or jog pair formed would contribute an entire layer to the loop side. If n_s were given by Equation 30, the resultant increase in the jog nucleation rate with loop size would lead to a growth rate which increased linearly with the size of the loop. This is clearly not the case, but we may not discard the possibility that the jogs move completely across the loop side in the time interval between jog nucleation events, because it is possible that the jogs nucleate preferentially at the loop corners. In this case the number of nucleation sites is not a function of the loop size. The presence of the stair rods at the loop corners is expected to result in a partial constriction of the stacking fault ribbon there, which would favor jog nucleation. Also, as shown schematically in Fig. 27, the formation of a jog at the corner would require the formation of only one stair rod dipole, rather than the two dipoles which are required to nucleate a pair of jogs on the loop side.

In the case where the rate of jog motion is not great enough to allow them to disappear at the loop corners before more are nucleated, they will disappear by meeting and annihilating opposite sign jogs moving in the other direction. Each jog then adds only a partial layer to the loop side, and so even though more jogs are nucleated per unit time on a longer loop side, the climb rate is independent of the side length. Thus we may distinguish two cases in which a constant growth rate may be expected in jog nucleation controlled growth. In the first case jog motion is very fast, and nucleation is concentrated at the corners. In the second case jog nucleation occurs all along the loop sides at a rate great enough to ensure that they do not all have time to travel to the loop corners before new jogs are nuclea ed. In both cases the loop growth rate Γ is proportional to the rate of jog nucleation J. The present work does not give us any means o determine which of these two cases is the real one, since we cannot directly observe the process of jog nucleation and motion. The jogs probably move by absorption of interstitials with a lower activation barrier than that for jog nucleation, but whether they move very quickly relative to the nucleation rate is uncertain. It is also not certain whether they nucleate preferentially at the loop corners.

The variation of Γ with the damage rate R is not simple. As R increases, Z, C_i', N, and ΔG^* all change. For the purpose of discussion consider the simple nucleation model discussed in section IV C. Clearly ΔG^* is a function of $\overline{G}_i$ through D^* (Equation 24). N, the number of sites adjacent to a critical nucleus, is also dependent on the size D^* of this nucleus, which varies with $\overline{G}_i$. Z, given by Equation 27, depends on $\partial^2 \Delta G/\partial i^2$, which will vary with $\overline{G}_i$. Finally, C_i', the interstitial concentration at the loop, is a function of R. At very low growth rates, C_i' may be equal to the interstitial concentration of the curves in Fig. 23, since very few interstitials are being absorbed a a concentration gradient due to the loop would not be expected. The effect of the strain field would tend to build an atmosphere of point defects at the loop so that C_i' may actually be somewhat great r than the average concentration in the foil. For higher growth rates a concentration gradient should be established as interstitials are absorbed at the loops, so that C_i' should be somewhat less than the average concentration.

In the absence of a more complete model for the jog nucleation process we cannot accurately predict the dependence of Z, N, and ΔG^* on $\overline{G}_1$. It is clear that if $\overline{G}_1$ is as insensitive to the beam current density as indicated in Tables II and III, ΔG^* must be a very strong function of $\overline{G}_1$. Since in the simple classical treatment of homogeneous loop nucleation (Hirth and Lothe,[31] pages 560–564) ΔG^* and the critical radius r* are not analytical functions of $\overline{G}$, we would not expect ΔG^* for the case of jog nucleation by Grilhe's model to be. Attempts to calculate ΔG^* from the curves in Fig. 17b, based on reasonable assumptions for the variables in the jog nucleation rate, yield curved lines on plots of log ΔG^* versus log $\overline{G}_1$, indicating that these are probably not simply related.

The observations of the present work may all be qualitatively explained by Grilhe's suggested model of jog nucleation. The activation energy for nucleation of loops in the bulk material should be larger than that for jog nucleation because jog nucleation is aided by the stress field of the existing dislocation loop. This was observed experimentally as the fact that it is possible to grow loops at a temperature at which it was no longer possible to nucleate loops due to the smaller supersaturation attainable at higher temperatures. The stacking fault energy is expected to have an effect on the values of both r_1 and r_2, so that regardless of the relative magnitudes of these quantities, lower stacking fault energies should increase the activation barrier for jog nucleation and thus loop growth. This is observed experimentally as an increase in the beam current density or supersaturation required for loop growth as stacking fault energy decreases.

Since the loop growth rate is controlled by the jog nucleation rate, the interstitial concentration at the loop is probably not too much less than that in the bulk of the foil, and once formed the jogs should travel quickly in this supersaturation. Their motion may involve the absorption of clusters of interstitials below the critical size necessary to nucleate new jogs.

Johnston et al.[68] have observed the passage of large superjogs along the sides of Frank loops in gold during annealing. The motion of such superjogs was slow enough to observe at successive stages only at the lowest annealing temperatures. In the present work many loops are observed to have what look like superjog pairs on some sides, but often these features remain during further growth, indicating that they do not contribute to growth (Fig. 5). The superjogs observed by Johnston et al. were of the order of 100 Å high, and it would be difficult to distinguish features of this size in the present experiment.

The large activation energy for jog nucleation is reflected in the observation that the loops do not shrink at measurable rates until quite high temperatures. Shrinkage would have to occur by vacancy absorption at the loops because of the high formation energy associated with emission of interstitials from the loops. The driving force for shrinkage is the reduction of the line energy of the loop rather than the reduction of any supersaturation of point defects. Measurements of the shrinkage rates of loops at different temperatures might yield an activation energy for jog formation which could be compared with the results of the present experiments.

Such experiments would have to be done using loops whose glide cylinders were parallel to the foil surface to prevent their loss to the surface by prismatic glide.

Factors affecting the growth rate Γ of different loops during the same irradiation may be divided into two main categories. First, there are a number of factors which may affect the width of the stacking fault ribbon. These include the stress, loop orientation, loop size, and temperature. The stress may vary with position in the foil. Loop orientation is a function of both stress and loop size. Loop size should not affect d once $L > d$, which is much smaller than the loop sizes measured in this work. Temperature is expected to be quite constant during a given irradiation ($\pm 5^\circ C$ or less).

The second category includes factors which affect the point defect concentration contributing to loop growth. These are depth in the foil, position in the beam, and possibly the proximity of other loops. Due to the point defect profiles in Fig. 23, loops at different depths in the foil should grow at different rates. Since most loops are not parallel to the foil surface, as they grow they should also grow into regions of different point defect concentration, possibly leading to faster growth of some sides of the loop. Pipe diffusion would reduce this effect, as would competition of loop sides for point defects. The proximity of other loops might affect the growth rate through competition for point defects, although definite evidence of this was not obtained, since careful stereo measurements would be necessary to establish loop proximity. Position in the beam has an effect on the damage rate through the beam profiles of Fig. 7, although care was taken to minimize this effect. All these factors contribute to scatter in measurements of the growth rate.

V. CONCLUSIONS

Nucleation and growth of prismatic interstitial loops was observed during irradiation in the HVEM at different temperatures and damage rates. The loops remained rhombus shaped throughout growth, with sides lying on {111} planes, suggesting low jog densities. Initially straight dislocations far away from edge orientation were observed to climb into helices with straight sides lying on {111} planes.

A minimum damage rate Φ_{min} was found to be necessary to induce growth at measurable rates. This, together with the low jog densities observed, was taken to indicate that climb was controlled by the rate of jog nucleation rather than by the rate of diffusion of point defects to the dislocations. Φ_{min} was found to be smaller for alloys of higher stacking fault energies, and this was attributed to the influence of stacking fault energy on the process of jog formation on extended dislocations. The growth rate was found to be constant for individual loops observed over a large size range.

The process of jog formation on extended dislocations has been discussed. The energies required to nucleate jogs by the formation of constrictions or by the direct formation of extended jogs are much larger than $\overline{G}_i$. Modification of the jog nucleation model of Fig. 26 by Grilhe[66] yields an activation energy for jog formation which is dependent on stacking fault energy. This model qualitatively agrees with the observations of this work.

Some evidence suggesting suppressed nucleation of certain loop orientations was observed. Although this may be relevant to some theories of irradiation creep,[6,7] a more systematic study, including analysis of the stress state in the foil, is needed.

Further work should include weak beam observations of the loop sides. A more complete study of the rotation of the loops would also be interesting. Annealing studies of loops whose glide cylinders are parallel to the foil surface should yield valuable information.

ACKNOWLEDGEMENTS

The author wishes to express his sincere gratitude for the continued guidance and support of Professor Jack Washburn. Thanks are also due to Professor J. Grilhe and to Krishna Seshan for helpful discussions of the jog nucleation problem. Bill Worthington's work in developing the hot stage is gratefully adknowledged, as well as David Howitt's assistance with the Faraday cup. Many thanks are due to my wife, Rosemary, for typing the manuscript.

This work was done under the auspices of the U. S. Energy Research and Development Administration through the Inorganic Materials Research Division of the Lawrence Berkeley Laboratory. Partial support was also generously provided by the General Electric Company.

REFERENCES

1. Proceedings of the 1971 International Conference on Radiation-Induced Voids in Metals, Albany, New York, edited by J. W. Corbett and L. C. Ianniello (U.S. Atomic Energy Commission, Oak Ridge, Tennessee, 1972).
2. D. I. R. Norris, Voids in Irradiated Metals (Part I), Rad. Effects 14, 1 (1972).
3. D. I. R. Norris, Voids in Irradiated Metals (Part II), Rad. Effects 15, 1 (1972).
4. S. D. Harkness and Che-Yu Li, A Study of Void Formation in Fast Neutron-Irradiated Metals, Met. Trans. 2, 1457 (1971).
5. M. F. Ashby, Summary: On Radiation-Enhanced Creep, Scripta Met. 6, 1231 (1972).
6. A. D. Brailsford and R. Bullough, Irradiation Creep Due to the Growth of Interstitial Loops, Phil. Mag. 27, 49 (1973).
7. G. W. Lewthwaite, Irradiation Creep Produced by the Effect of Stress on the Nucleation of Dislocation Loops, Phil. Mag. 28, 1287 (1973).
8. J. H. Gittus, Theory of Irradiation-Induced Primary Creep in Crystalline Solids, Phil. Mag. 29, 679 (1974).
9. J. H. Gittus, Theory of Dislocation-Creep for a Material Subjected to Bombardment by Energetic Particles, Phil. Mag. 28, 261 (1973).
10. J. H. Gittus, Theory of Dislocation-Creep Due to the Frenkel Defects or Interstitialcies Produced by Bombardment with Energetic Particles, Phil. Mag. 25, 345 (1972).

11. J. O. Stiegler and E. E. Bloom, Void Formation in Irradiated Nickel 270, Rad. Effects 8, 33 (1971).

12. A. Jostsons and E. L. Long, Jr., Radiation Damage and the Effects of Postirradiation Annealing in 1100 Grade Aluminum, Rad. Effects 16, 83 (1972).

13. K. Farrell, A. Wolfenden, and R. T. King, The Effects of Irradiation TEmperature and Preinjected Gases on Voids in Aluminum, Rad. Effects 8, 107 (1971).

14. D. J. H. Cockayne (Electron Microscope Unit, The University of Sydney, Sydney, Australia), private communication, February 1975.

15. G. L. Kulcinski, J. J. Laidler, and D. G. Doran, Simulation of High Fluence Fast Neutron Damage with Heavy Ion Bombardment, Rad. Effects 7, 195 (1971).

16. G. L. Kulcinski, J. L. Brimhall, and H. E. Kissinger, Production of Voids in Pure Metals by High Energy Heavy Ion Bombardment, in Proceedings of the 1971 International Conference on Radiation-Induced Voids in Metals, Albany, New York (U.S. Atomic Energy Commission, Oak Ridge, Tennessee, 1972), 449.

17. H. H. Neely and K. Herschbach, Void Formation in Nickel During High Temperature Proton Irradiation, Rad. Effects 7, 187 (1971).

18. C. W. Chen, A. Mastenbroek, and J. D. Elen, An Electron Stereomicroscopy Analysis of Voids Produced in Nickel During Ion Irradiation, Rad. Effects 16, 127 (1972).

19. J. A. Hudson, D. J. Mazey, and R. S. Nelson, Void Formation in Nickel During 20 MeV C^{++} Irradiation at 525°C, J. Nucl. Matls. 41, 241 (1971).

20. D. I. R. Norris, The Growth of Voids in Nickel in a High-Voltage Electron Microscope, Phil. Mag. 23, 135 (1971).

21. D. I. R. Norris, The Use of the High Voltage Electron Microscope to Simulate Fast Neutron-Induced Void Swelling in Metals, J. Nucl. Matls. 40, 66 (1971).

22. M. J. Makin, Void Nucleation During Electron Irradiation, Phil. Mag. 25, 761 (1972).

23. P. Rao, L. D. Glowinski, and P. S. Ho, Effect of Electron-Irradiation on Void Formation in Helium-Pre-injected Aluminium Films, Phil. Mag. 27, 341 (1973).

24. K. R. Williams and S. B. Fisher, The Void Swelling of a γ'-Hardened Alloy, Rad. Effects 15, 243 (1972).

25. M. W. Thompson, Defects and Radiation Damage in Metals (Cambridge University Press, Cambridge, 1969).

26. L. T. Chatterton, Radiation Damage in Crystals (Methuen & Co. Ltd., London, 1965).

27. D. I. R. Norris, Depth Distributions of Vacancy Clusters in Ion Bombarded Gold and Nickel, Phil. Mag. 19, 653 (1969).

28. L. E. Thomas, T. Schober, and R. W. Balluffi, Defects Observed by Electron Microscopy in Gold Bombarded with keV Gold Ions: I. Nature of Defects, Rad. Effects 1, 257 (1969).

29. L. E. Thomas, T. Schober, and R. W. Balluffi, Defects Observed by Electron Microscopy in Gold Bombarded with keV Gold Ions: II. Mechanism of Defect Formation, Rad. Effects 1, 269 (1969).

30. T. Schober, L. E. Thomas, and R. W. Balluffi, Defects Observed by Electron Microscopy in Gold Bombarded with keV Gold Ions: III. Stereo Study of Subcascade Cluster Geometries, Rad. Effects 1, 279 (1969).

31. J. P. Hirth and J. Lothe, Theory of Dislocations (McGraw-Hill Book Company, New York, 1968).

32. J. Friedel, Dislocations (Pergamon Press, Oxford, 1964).

33. G. Das and J. Washburn, On the Orientation of Perfect Prismatic Dislocation Loops in Pure Aluminum, Appl. Phys. Lett. 5, 151 (1964).

34. G. Das and J. Washburn, Defects Formed from Excess Vacancies in Aluminum, Phil. Mag. 11, 955 (1965).

35. T. Hasegawa, K. Asou, and S. Karashima, Electron Microscope Study of Stacking Fault Energies in Cu-11.5 and 16.0 At. Pct Al Alloys at Temperatures Between 20 and 700°C, Met. Trans. 5, 933 (1974).

36. K. Urban, Growth of Defect Clusters in Thin Nickel Foils During Electron Irradiation (I), Phys. Stat. Sol. (a) 4, 761 (1972).

37. S. B. Fisher, Electron Radiation Damage in Copper in the High Voltage Electron Microscope, Rad. Effects 7, 173 (1971).

38. M. Ipohorski and M. S. Spring, Electron Radiation Damage in a High Voltage Electron Microscope, Phil. Mag. 20, 937 (1969).

39. M. Kiritani and N. Yoshida, Formation and Annihilation of Point Defect Clusters in Metals Irradiated by 3 MV Electron Microscope, Cryst. Latt. Defects 3, 83 (1973).

40. L. M. Brown, On Electron Radiation Damage in Crystals, Phil. Mag. 19, 869 (1969).

41. M. J. Makin, A Simple Theory of Loop Formation and Enhanced Diffusion in Crystals Examined by High Voltage Electron Microscopy, Phil. Mag. 20, 1133 (1969).

42. D. I. R. Norris, Dislocation Loop Growth in an Electron Irradiated Thin Foil, Phil. Mag. 22, 1273 (1970).

43. K. Urban and M. Wilkens, Growth of Defect Clusters in Thin Nickel Foils During Electron Irradiation: II. Temperature Dependence of the Growth Rate of Interstitial Loops, Phys. Stat. Sol. (a) 6, 173 (1971).

44. Y. Adda, Report on the CEA Program of Investigations of Radiation-Induced Cavities in Metals: Presentation of Some Results, in Proceedings of the 1971 International Conference on Radiation-Induced Voids in Metals, Albany, New York (U.S. Atomic Energy Commission, Oak Ridge, Tennessee, 1972), 31.

45. J. L. Brimhall, H. E. Kissinger, and G. L. Kulcinski, The Effect of Temperature on Void Formation in Irradiated Pure and Impure Metals, in Proceedings of the 1971 International Conference on Radiation-Induced Voids in Metals, Albany, New York (U.S. Atomic Energy Commission, Oak Ridge, Tennessee, 1972), 338.

46. A. Wolfenden, High Fluence Neutron Irradiation Damage in Copper-10 Wt % Aluminum and Copper, Rad. Effects 15, 255 (1972).

47. V. Levy, J. Mathie, A. Risbet, R. Levy, and J. Poirier, European Conference on Voids Formed by Irradiation of Reactor Materials, Reading, England, 1971.

48. D. Howitt, The Measurement of Radiation Damage in Organic Crystals in the Range of Electron Energy between 200 keV and 650 keV, (M. S. thesis) LBL-3180, December 1974.

49. W. Worthington, T. Kosel, and R. Sinclair, Proceedings of the 32nd Annual Meeting of the Electron Microscopy Society of America, St. Louis, Missouri, 1974 (Claitor's Publishing Division, Baton Rouge, La., 1974).

50. P. B. Hirsch, A. Howie, R. B. Nicholson, D. W. Pashley, M. J. Whelan, Electron Microscopy of Thin Crystals (Butterworths, London, 1965).

51. R. Bullough and A. J. E. Foreman, The Elastic Energy of a Rhombus-Shaped Dislocation Loop, Phil. Mag. 9, 314 (1964).

52. A. Howie and P. R. Swann, Direct Measurements of Stacking-Fault Energies from Observations of Dislocation Nodes, Phil. Mag. 6, 1215 (1961).

53. A. J. E. Foreman, The Diffusion of Point Defects to the Foil Surface During Irradiation Damage Experiments in the High Voltage Electron Microscope, Rad. Effects 14, 175 (1972).

54. O. S. Oen, Cross Sections for Atomic Displacements in Solids by Fast Electrons, ORNL-3813, Oak Ridge National Laboratory, May 1965.

55. Physical Metallurgy, edited by R. W. Cahn (American Elsevier, New York, 1970), Chapter 14.

56. C. Kittel, Introduction to Solid State Physics (John Wiley and Sons, Inc., New York, 1953), 568.

57. A. C. Damask and G. J. Dienes, Point Defects in Metals (Gordon and Breach, New York, 1963), 31.

58. D. Kuhlmann-Wilsdorf, The Growth and Annealing of Stacking Fault Tetrahedra, Acta Met. 13, 257 (1965).

59. A. N. Stroh, Constrictions and Jogs in Extended Dislocations, Proc. Phys. Soc. London B67, 427 (1954).

60. C. B. Carter and I. L. F. Ray, Observations of Constrictions on Dissociated Dislocation Lines in Copper Alloys, Phil. Mag. 29, 1231 (1974).

61. R. S. Barnes, The Climb of Edge Dislocations in Face-Centered Cubic Crystals, Acta Met. 2, 380 (1954).

62. H. Kimura, R. Maddin, and D. Kuhlmann-Wilsdorf, Quenched-in Vacancies in Noble Metals: II. Mechanism of Quench Hardening, Acta Met. 7, 154 (1959).

63. R. M. Thomson and R. W. Balluffi, Kinetic Theory of Dislocation Climb: I. General Models for Edge and Screw Dislocations, J. Appl. Phys. 33, 803 (1962).

64. B. Escaig, Emission et Absorption de Défauts Ponctuels par les Dislocations Dissociées, Acta Met. 11, 595 (1963).

65. J. Grilhe and K. Seshan (Inorganic Materials Research Division, Lawrence Berkeley Laboratory, and Department of Materials Science and Engineering, University of California, Berkeley, California), work in progress.

66. J. Grilhe (Inorganic Materials Research Division, Lawrence Berkeley Laboratory, and Department of Materials Science and Engineering, University of California, Berkeley, California), work in progress.

67. J. Feder, K. C. Russell, J. Lothe, and G. M. Pound, Homogeneous Nucleation and Growth of Droplets in Vapours, Adv. Phys. 15, 111 (1966).

68. I. A. Johnston, P. S. Dobson, and R. E. Smallman, The Role of Jog Nucleation and Propagation in the Annealing of Faulted Loops in Low Stacking Fault Energy Metals, Cryst. Latt. Defects 2, 133 (1971).

FIGURE CAPTIONS

Fig. 1. Characteristic "black dot" defects produced at room temperature.

Fig. 2. Schematic drawing of an extended rhombus shaped prismatic loop.

Fig. 3. Loops grown in Cu-3.5 wt. % Al at 300°C with ϕ = .061 amps/cm^2

a) $\vec{g} = \bar{1}11$

b) Thompson tetrahedron and projected shapes of pure edge rhombus loops for Fig. 3a. The beam is 4° off <110>.

c) $\vec{g}$ = 002, same area.

Fig. 4. Loops grown in a 111 oriented foil, 7.5 wt. % Al.

a) $\vec{g} = 2\bar{2}0$, $s > 0$.

b) $\vec{g} = \bar{2}20$, $s > 0$.

Fig. 5. Loops which exhibit irregularities.

a) A loop which develops a very large pair of superjogs on one side.

b) A loop which develops an irregular shape and then reverts to the more regular shape.

c), d) Loops which develop a number of superjogs at one corner.

Fig. 6. Loops grown in a focussed beam, 300°C, 3.5 wt. % Al.

Fig. 7. Beam profiles for focussed and defocussed beams.

Fig. 8. Plots of loop sizes versus time.

a) 1.0 wt. % Al, 300°C, ϕ = .043 amps/cm^2

b) 3.5 wt. % Al, 300°C, ϕ = .081 amps/cm^2

c) 3.5 wt. % Al, 300°C, ϕ = .061 amps/cm^2

d) 7.5 wt. % Al, 300°C, Φ = .035 amps/cm^2.

e) 1.0 wt. % Al, 450°C, Φ = .020 amps/cm^2.

f) 3.5 wt. % Al, 450°C, Φ = .016 amps/cm^2.

g) 7.5 wt. % Al, 450°C, Φ = .049 amps/cm^2.

Fig. 9. Growth series of the loops of Fig. 8a.

Fig. 10. Growth series of the loops of Fig. 8b.

Fig. 11. Growth series of the loops of Fig. 8c.

Fig. 12. Growth series of the loops of Fig. 8d.

Fig. 13. Growth series of the loops of Fig. 8e.

Fig. 14. Growth series of the loops of Fig. 8f.

Fig. 15. Growth series of the loops of Fig. 8g.

Fig. 16. Plots of loop size versus time for a few individual loops. In the plots which show two lines, the upper line is for the loop sides lying in edge-on {111} planes.

a), b), c) Cu-3.5 wt. % Al, 300°C.

d), e), f) Cu-7.5 wt. % Al, 300°C.

Fig. 17. Plots of the growth rate Γ versus the damage rate Φ for 300°C (a) and 450°C (b).

Fig. 18. Geometry for calculation of the loop rotation under stress.

Fig. 19. a) Loop energy versus ϕ for rotation about the <100> major axis.

b) Plot of the stress required to hold a loop at a given orientation for rotation about the <100> major axis.

c) Stress versus ϕ for rotation about the <110> minor axis.

d) Loop energy versus ϕ for rotation about the <110> minor axis.

Fig. 20. a) Two loops which have concave projected shapes; one is nearly edge on.

b) Typical convex loop images.

Fig. 21. The projected shapes of inclined loops viewed exactly along [110] for different values of ϕ.

Fig. 22. A series of micrographs of a loop which rotates as it grows under an approximately constant stress. Note that the loop on the right slips out of the foil leaving a shadow image in d).

Fig. 23. The variation of the normalized vacancy concentration with depth in the foil for different values of the parameter f.

Fig. 24. a) An extended jog pair.

b) A constricted jog pair.

Fig. 25. a) A triangular jog nucleus on an extended dislocation.

b) The triangular nucleus with stair rod dipoles.

c) The completed form of Fig. 25b.

Fig. 26. Formation of a pair of jogs on an extended dislocation by the growth of a rectangular jog nucleus.

a) A row of point defects along one Shockley dislocation.

b) Collapse of the configuration to a perfect loop.

c) Extension of the perfect loop.

Fig. 27. An extended superjog nucleated at a loop corner.

XBB 755-3987

Fig. 1

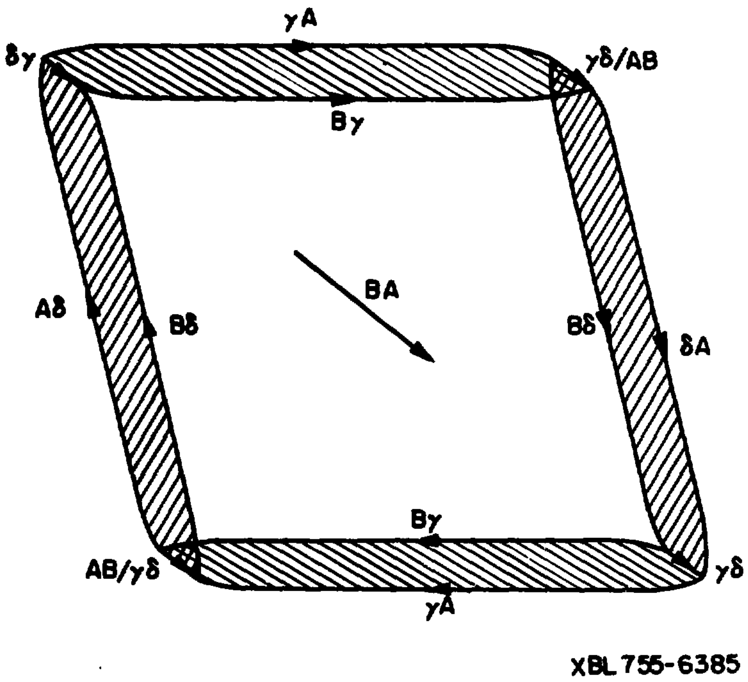

Fig. 2

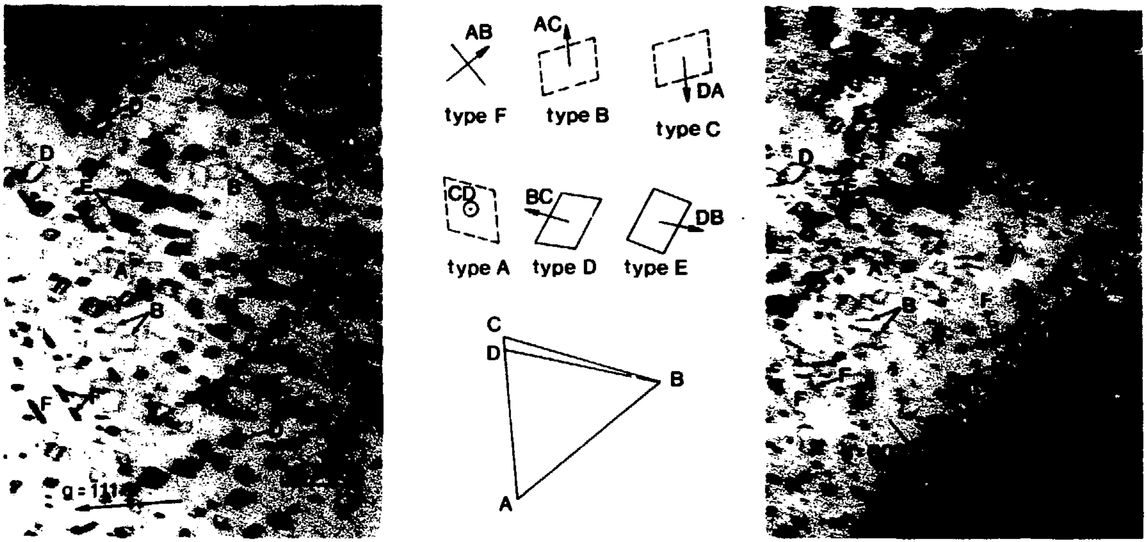

a b c

XBB 755-3989

Fig. 3

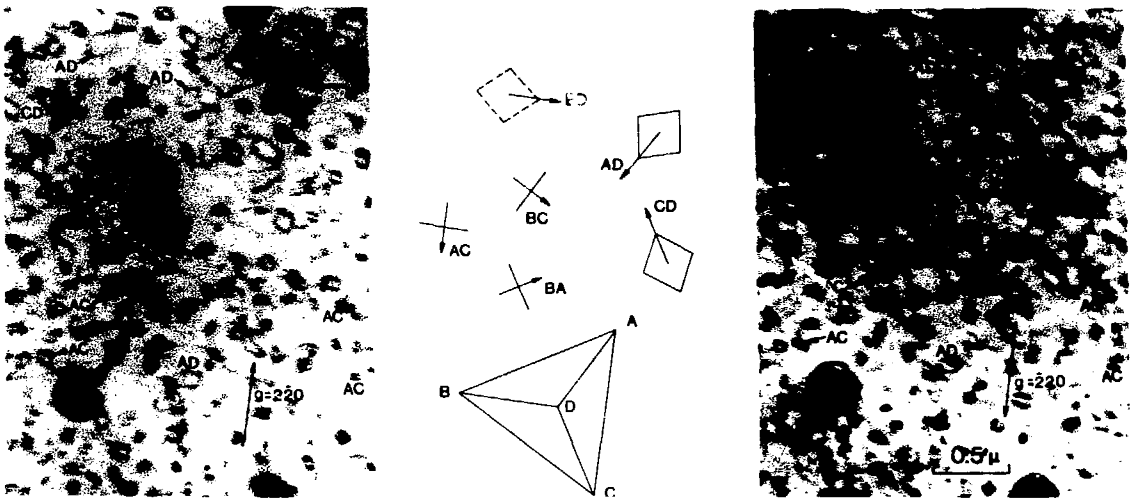

a b

XBB 755-3990

Fig. 4

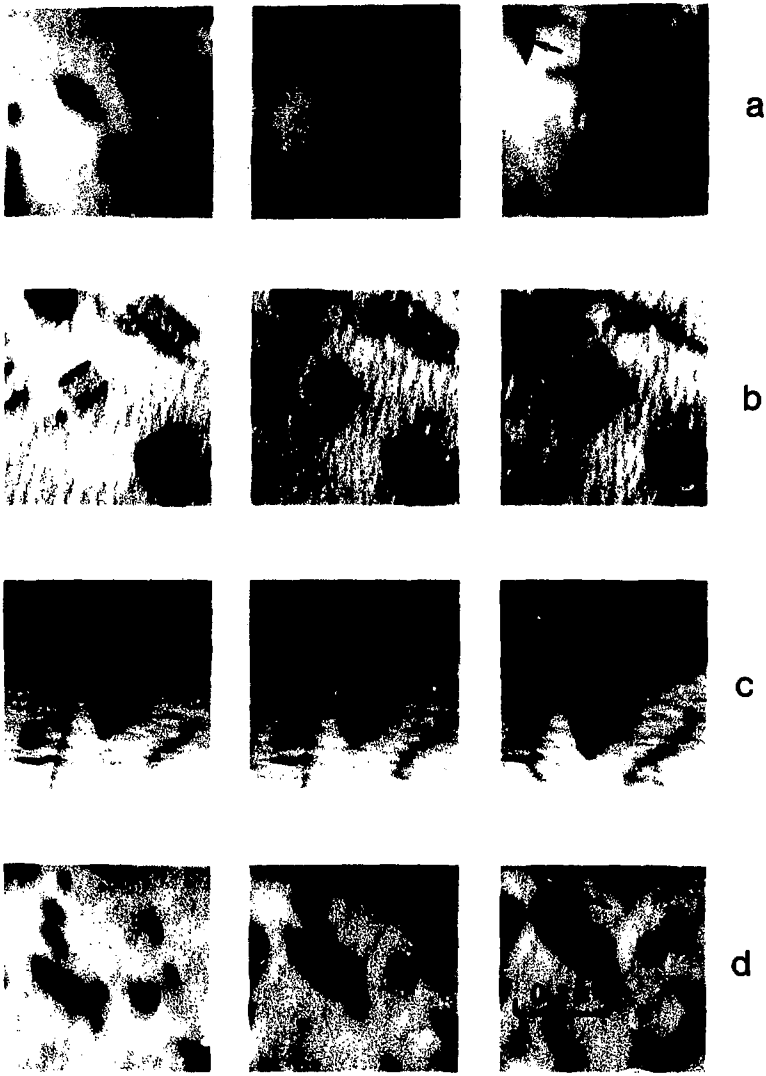

XBB 755-3995

Fig. 5

XBB 755-3986

Fig. 6

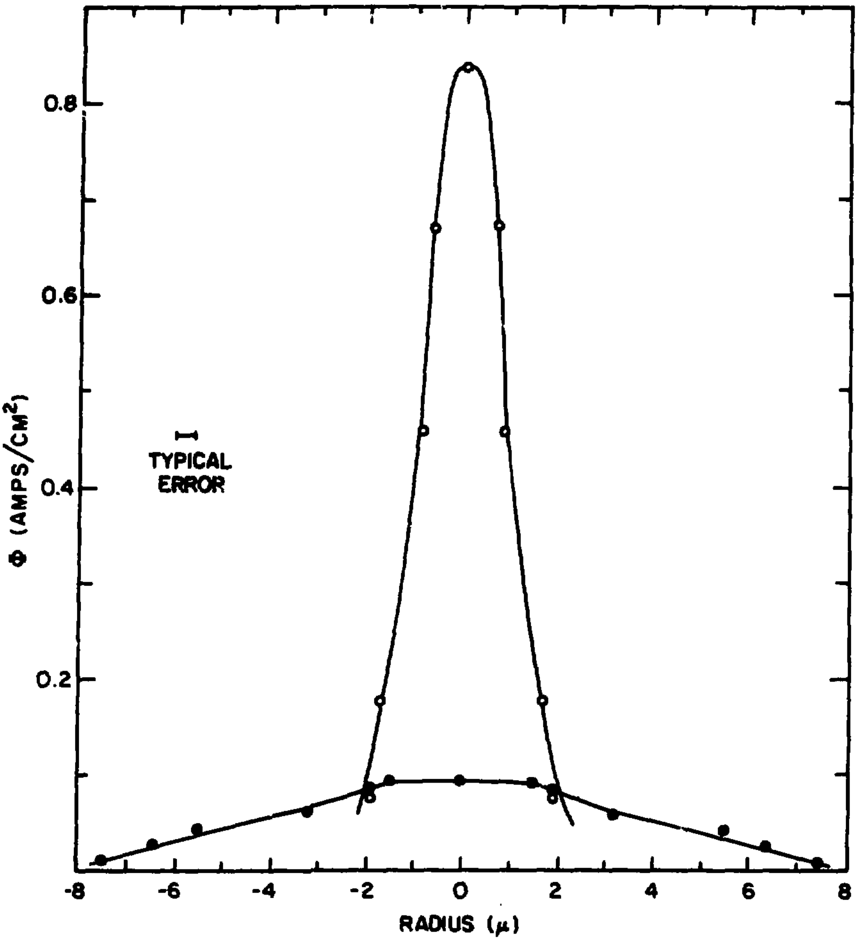

XBL 755-6373

Fig. 7

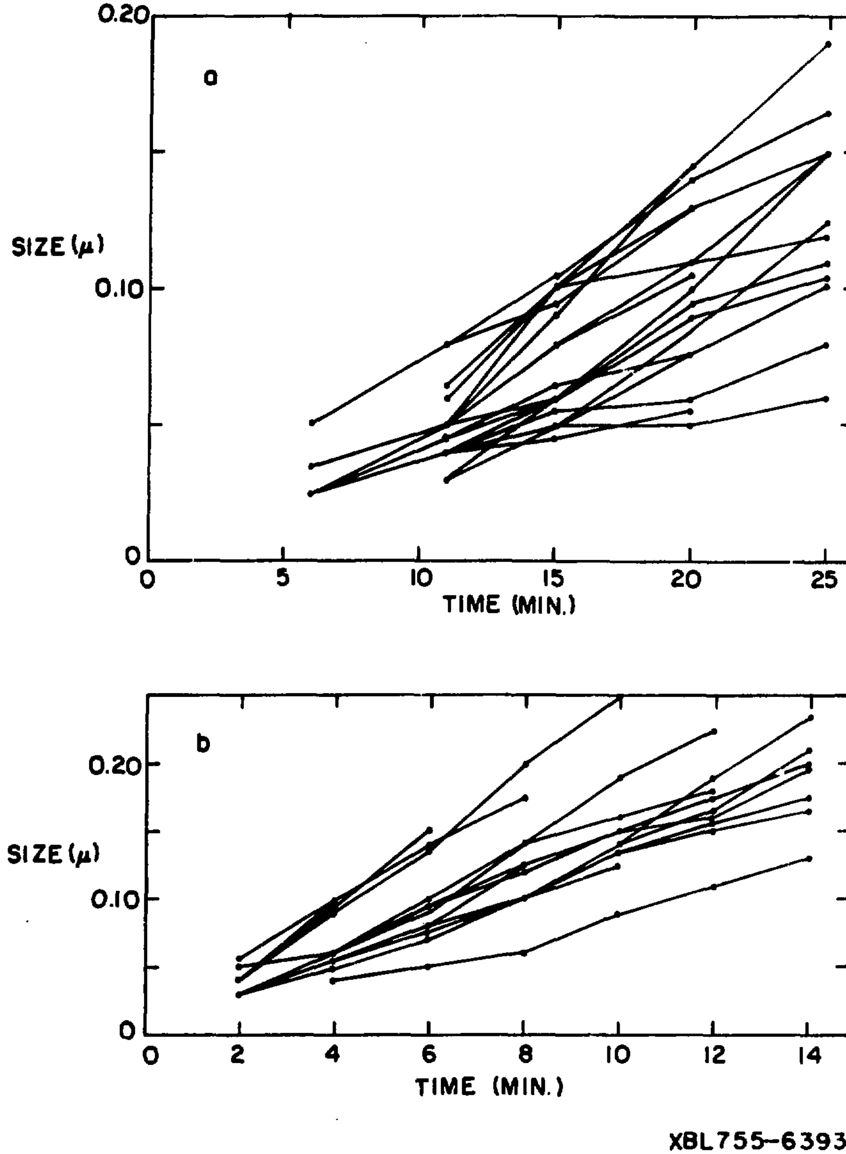
a
0.20
SIZE (μ)
0.10
0
0
5
10
15
20
25
TIME (MIN.)
b
0.20
SIZE (μ)
0.10
0
0
2
4
6
8
10
12
14
TIME (MIN.)
XBL755-6393

Fig. 8

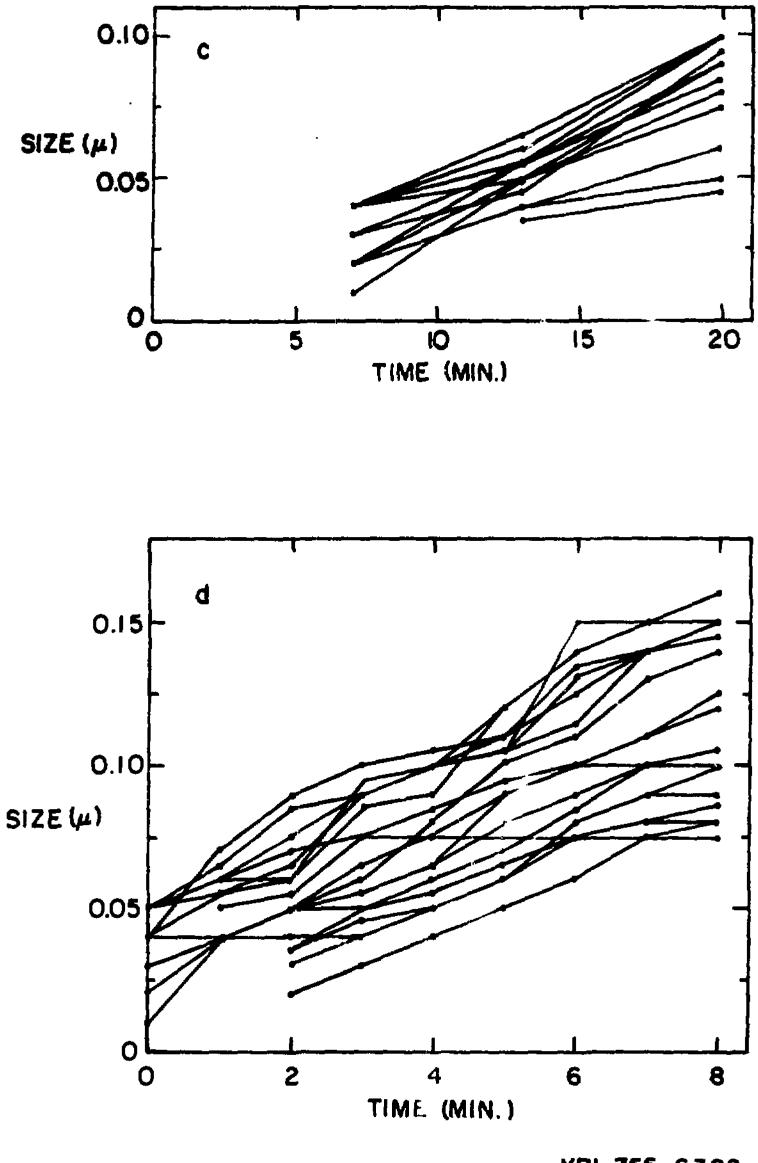
c
SIZE (μ)
0.10
0.05
0
0
5
10
15
20
TIME (MIN.)
d
SIZE (μ)
0.15
0.10
0.05
0
0
2
4
6
8
TIME (MIN.)
XBL 755-6392

Fig. 8 cont.

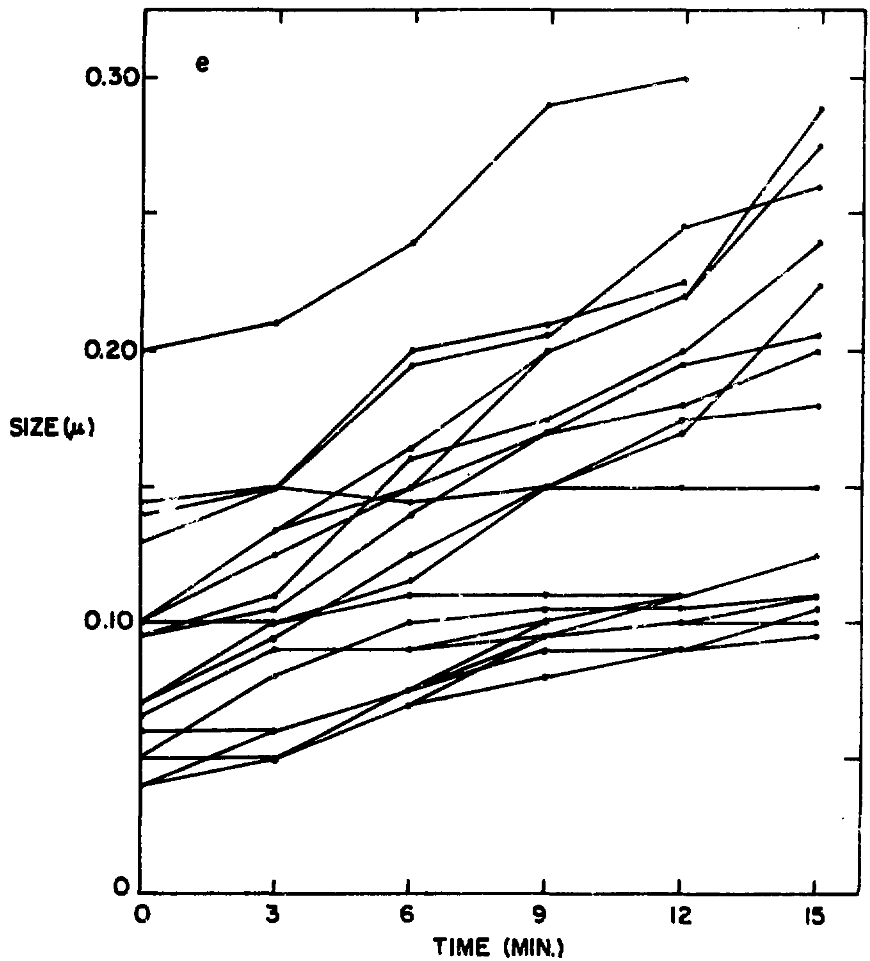

XBL 755-6391

Fig. 8 cont.

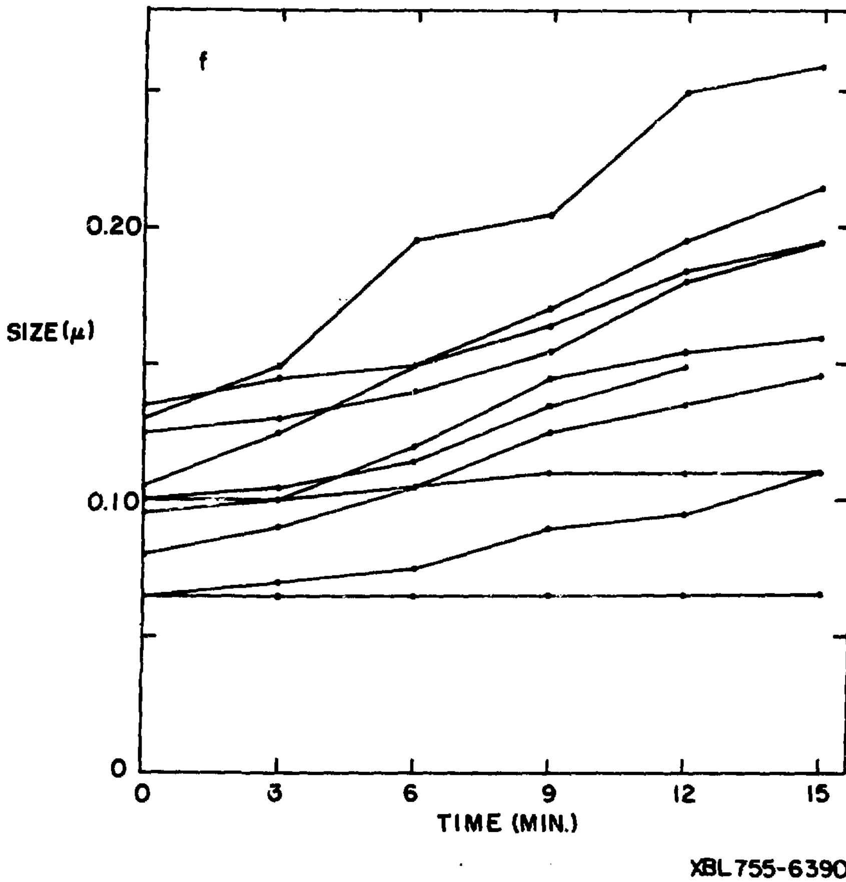

Fig. 8 cont.

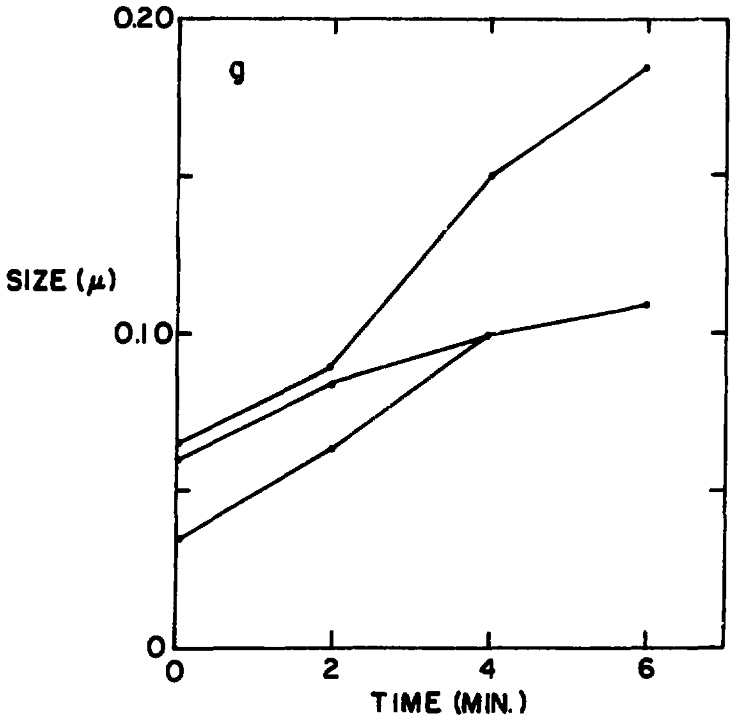

XBL755-6389

Fig. 8 cont.

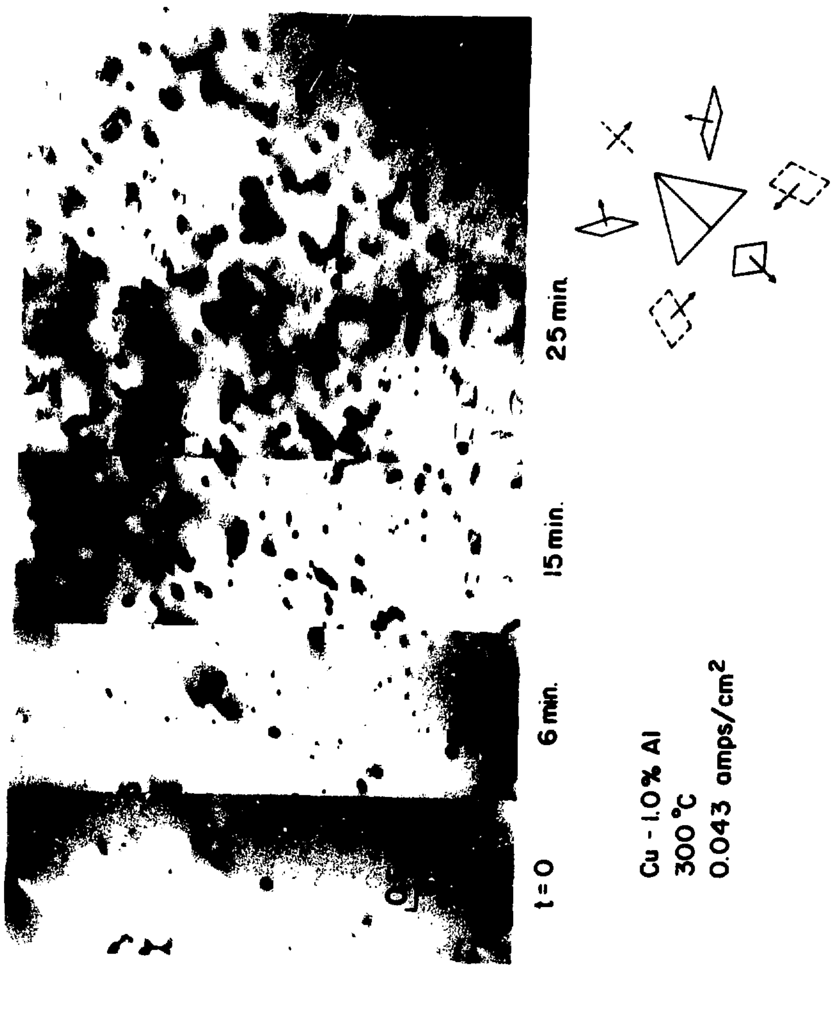

XBB 755-3993

Fig. 9

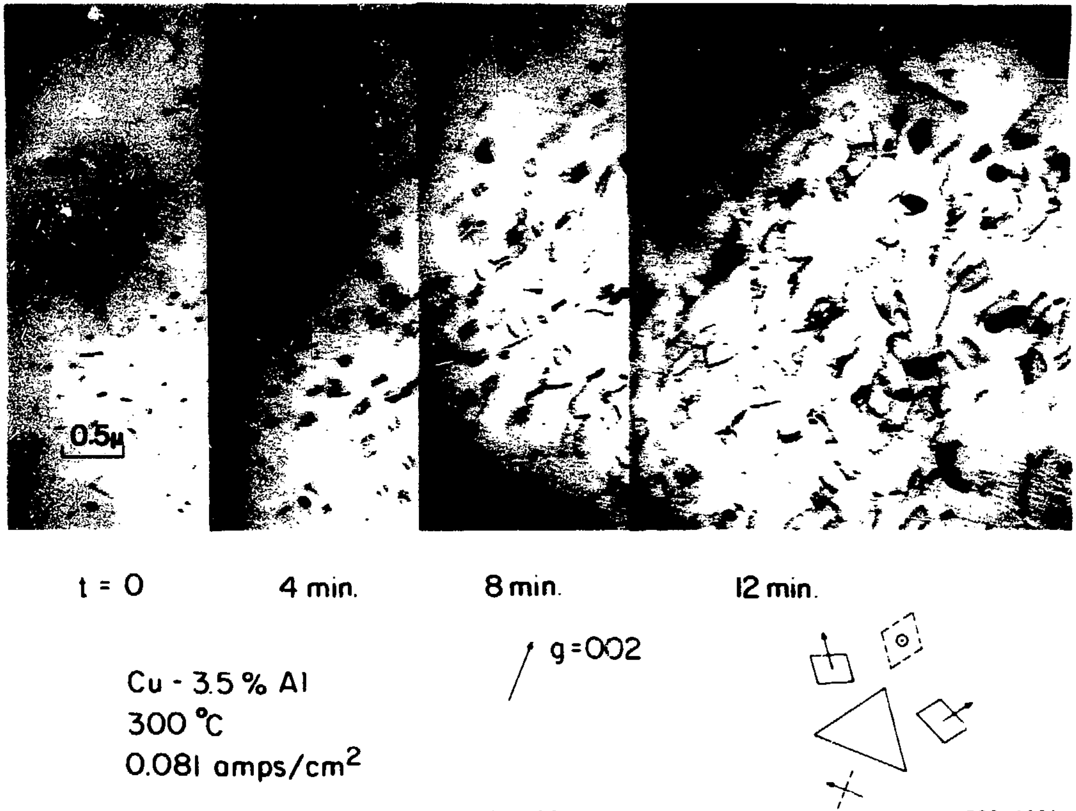

Fig. 10

XBB 755-3994

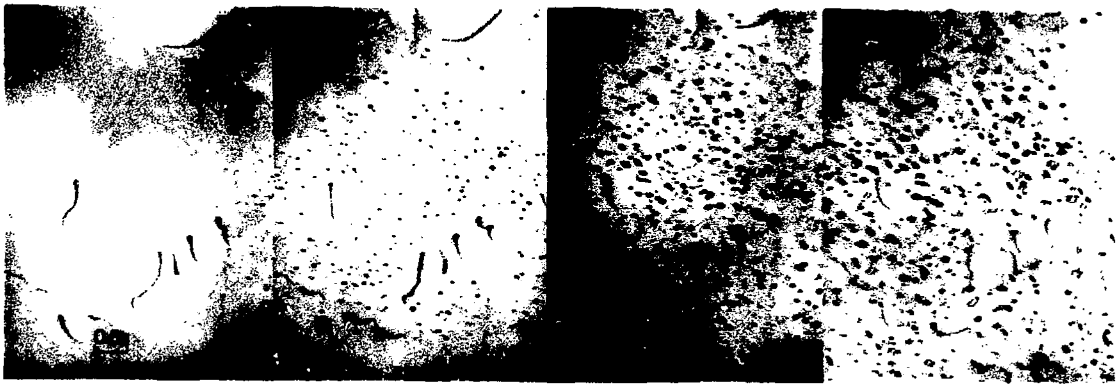

Cu - 3.5 % Al
300 °C
0.061 amps/cm^2

$g = \bar{1}11$

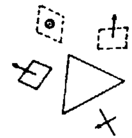

XBB 755-3979

Fig. 11

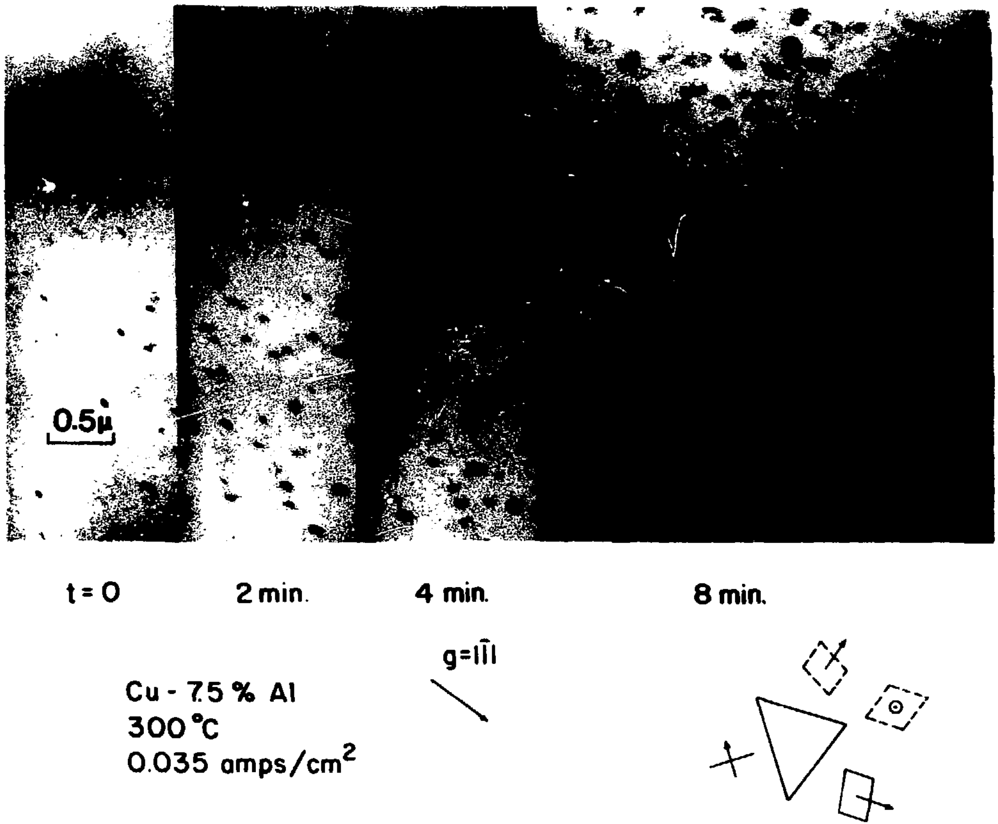

Fig. 12

XBB 735-3992

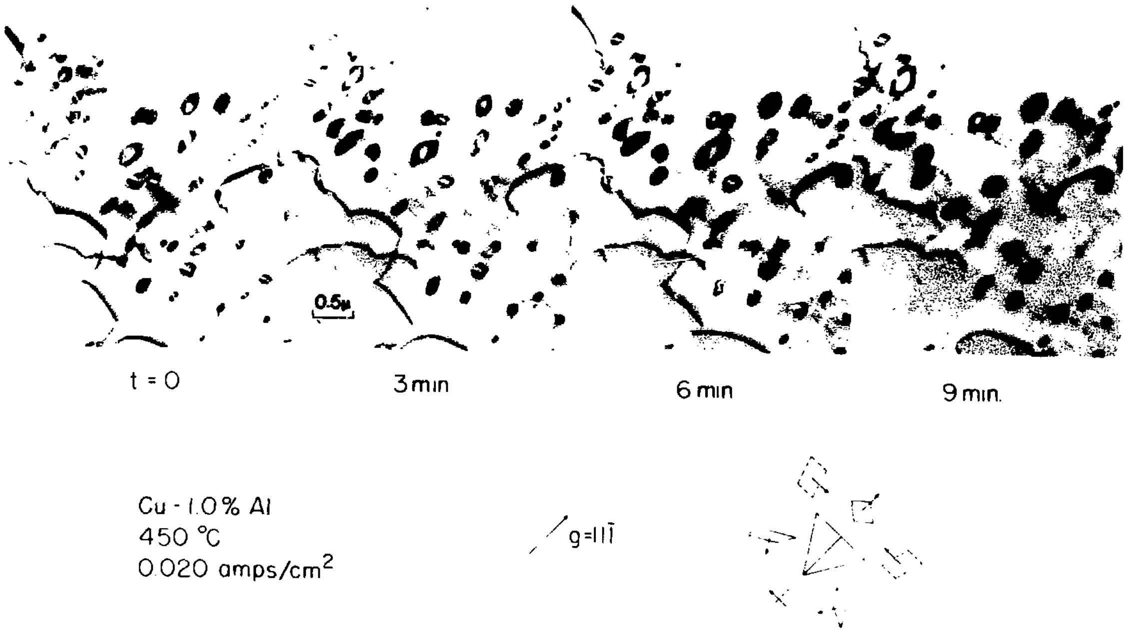

XBB 755-3981

Fig. 13

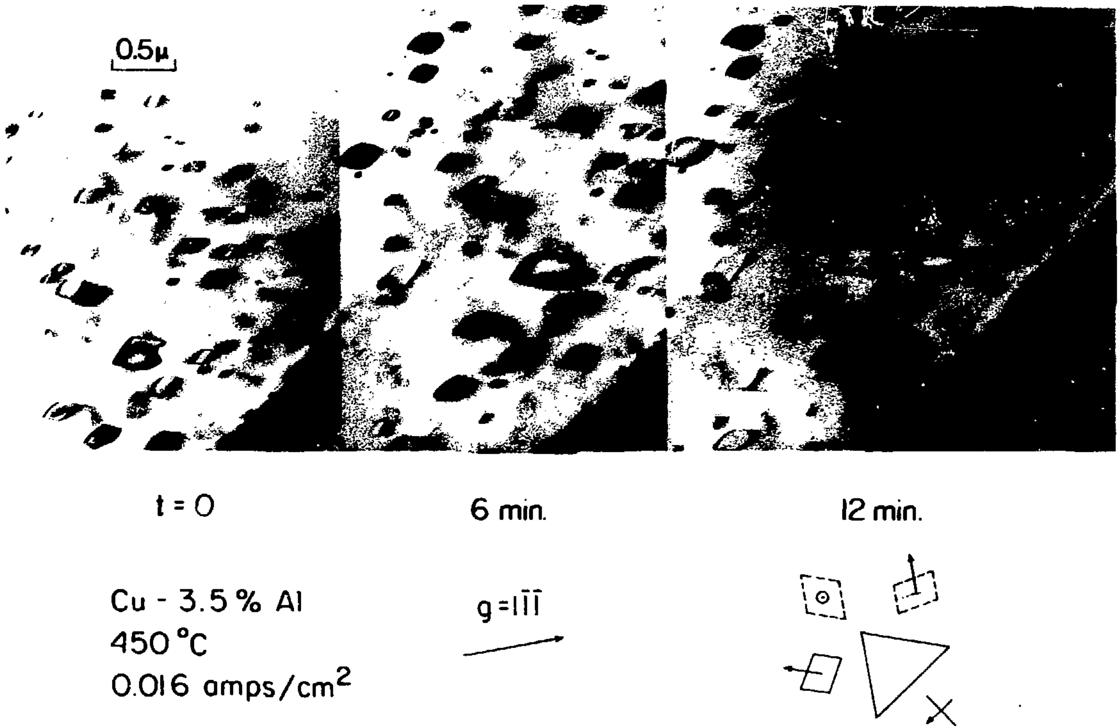

Fig. 14

XBB 755-3980

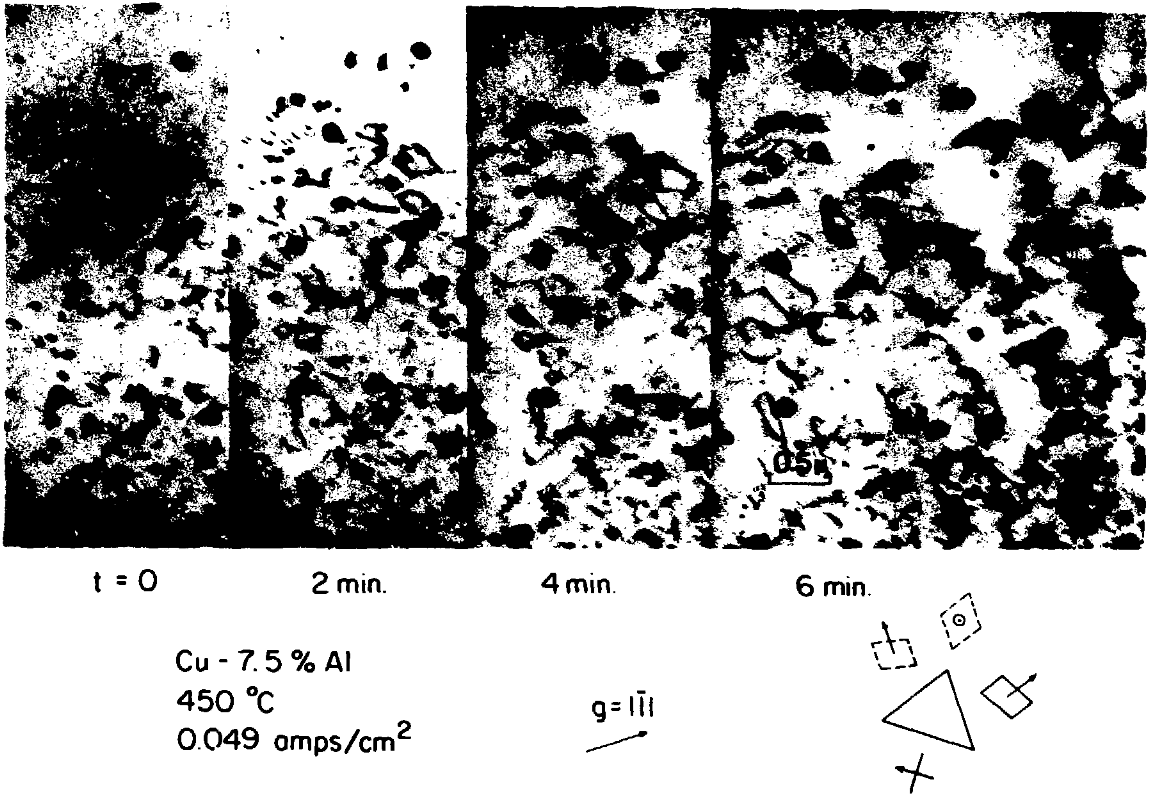

Fig. 15

XBB 755-3991

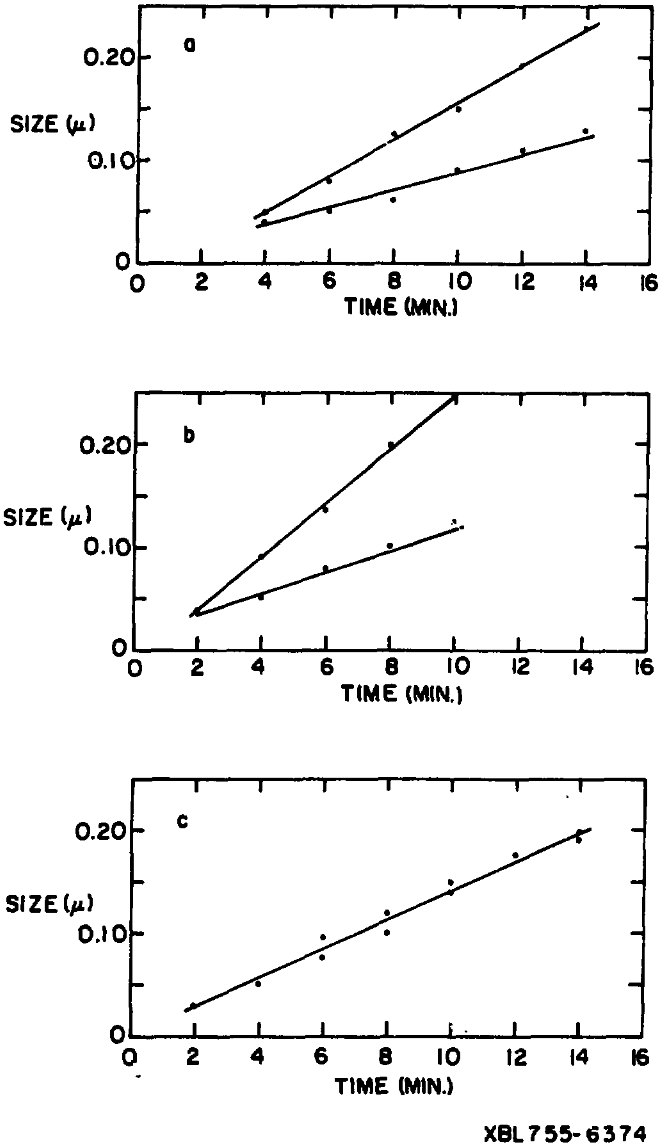

Fig. 16

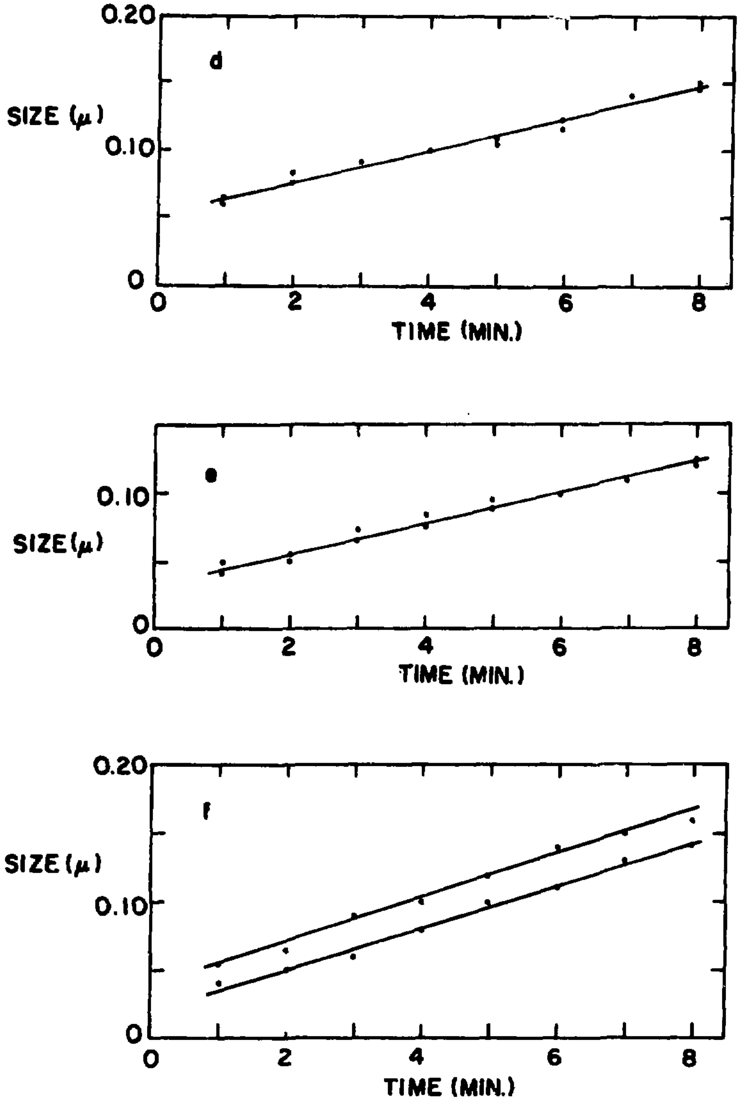

XBL755-6375

Fig. 10 cont.

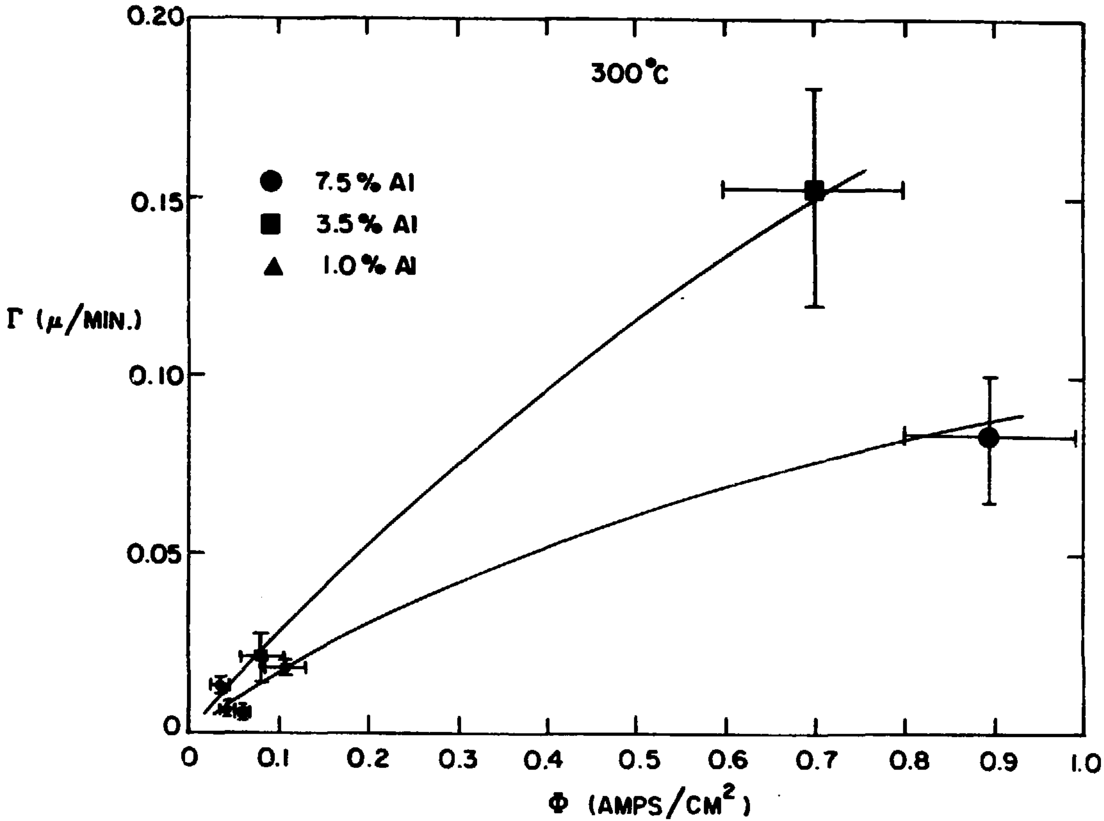

a

XBL755-6376

Fig. 17

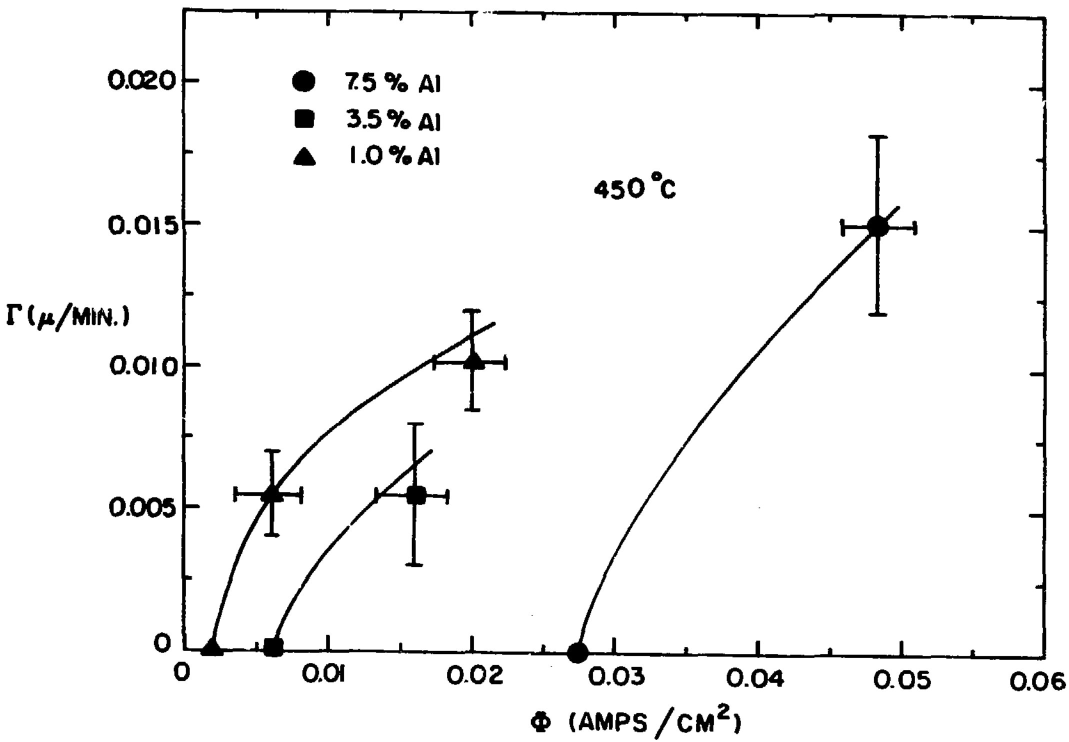

b

XBL 755-6377

Fig. 17 cont.

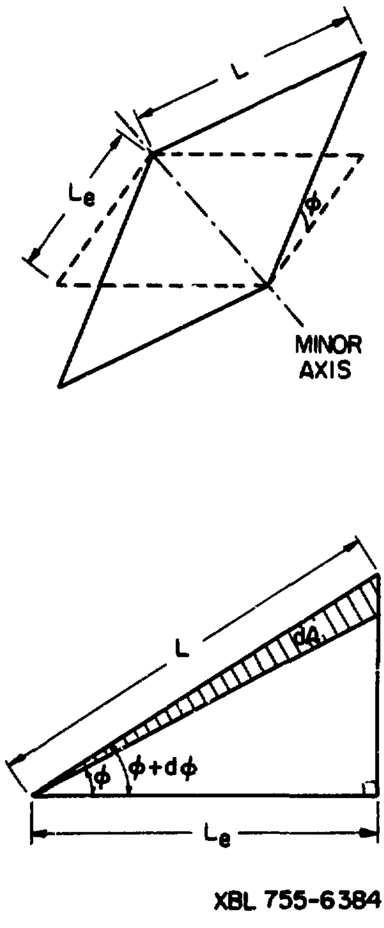

Fig. 18

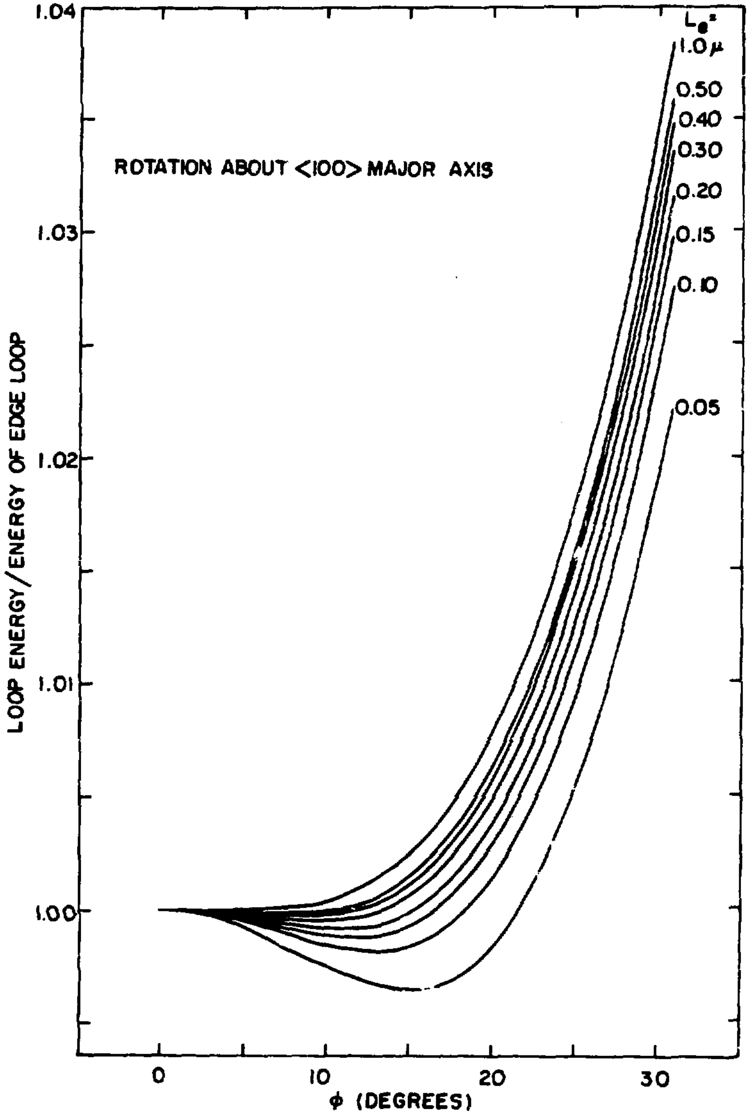

a

XBL755-6378

Fig. 19

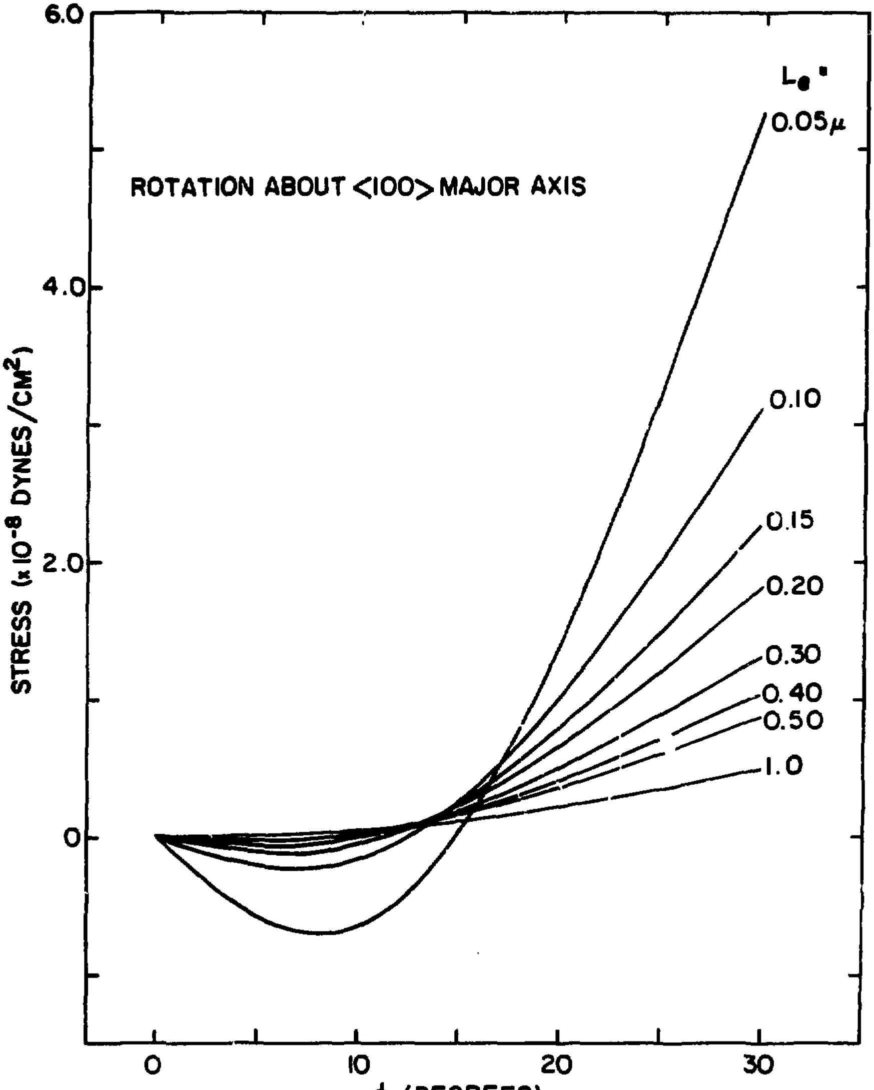

b

XBL 755-6379

Fig. 19 cont.

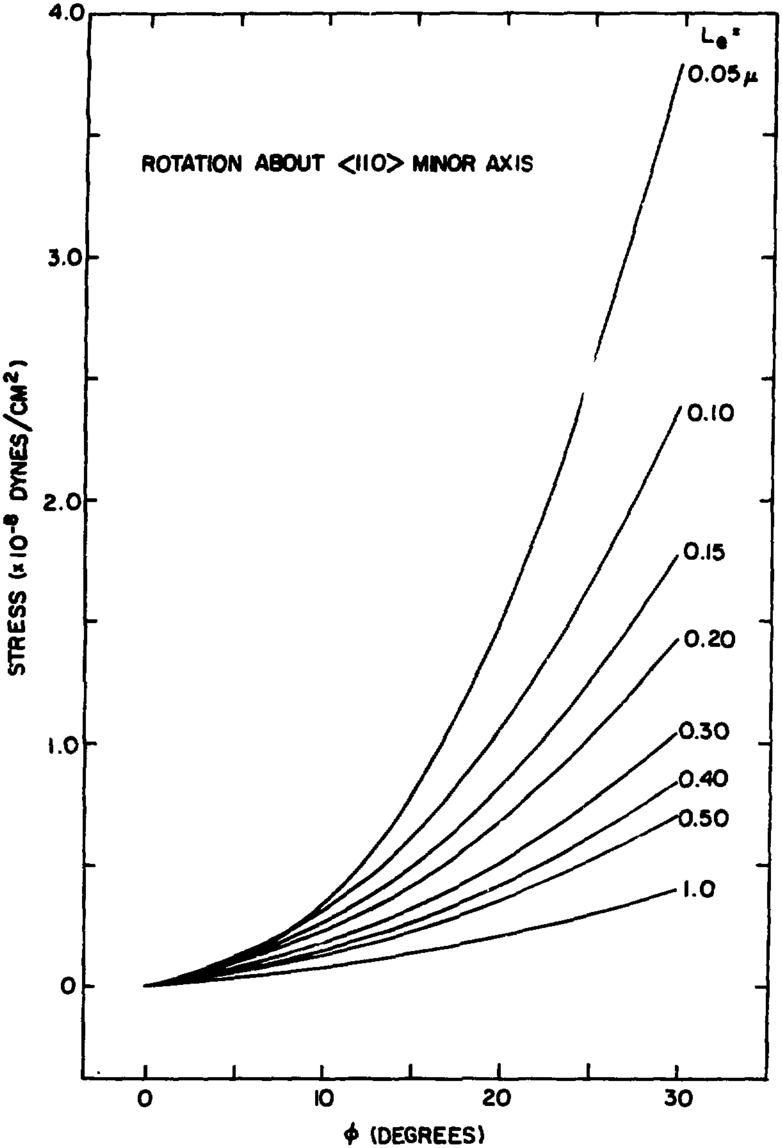

c

XBL 755-6380

Fig. 19 cont.

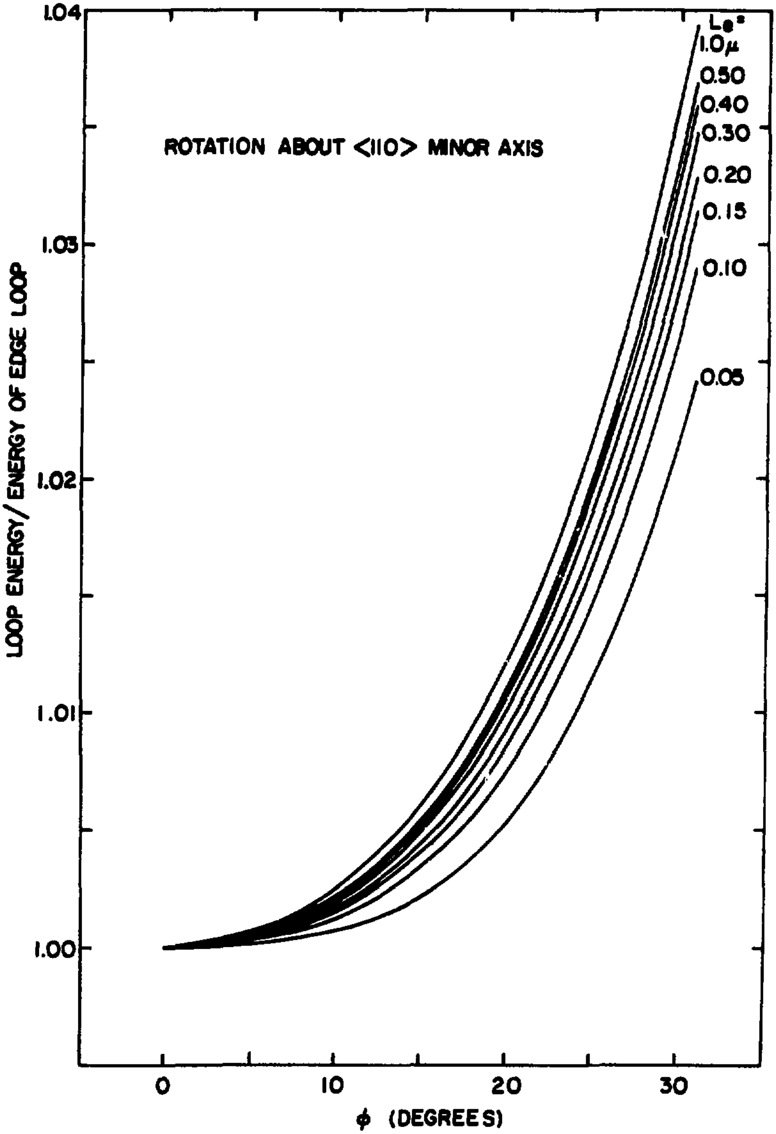

d

XBL755-6381

Fig. 19 cont.

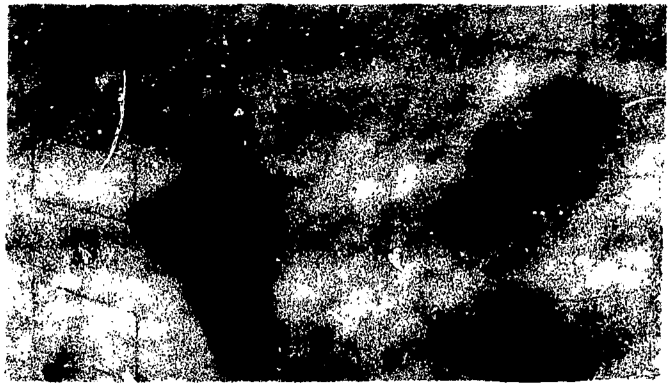

a

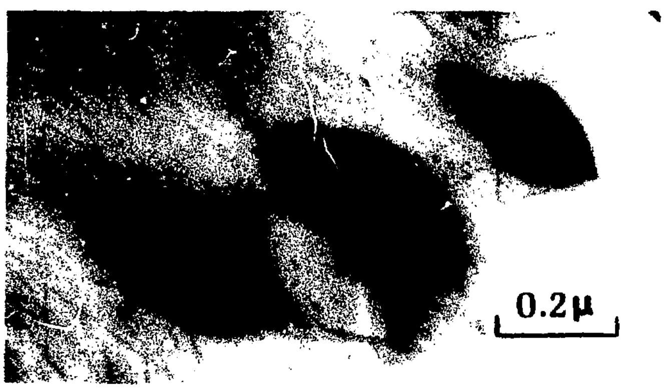

XBB 755-3988

b

Fig. 20

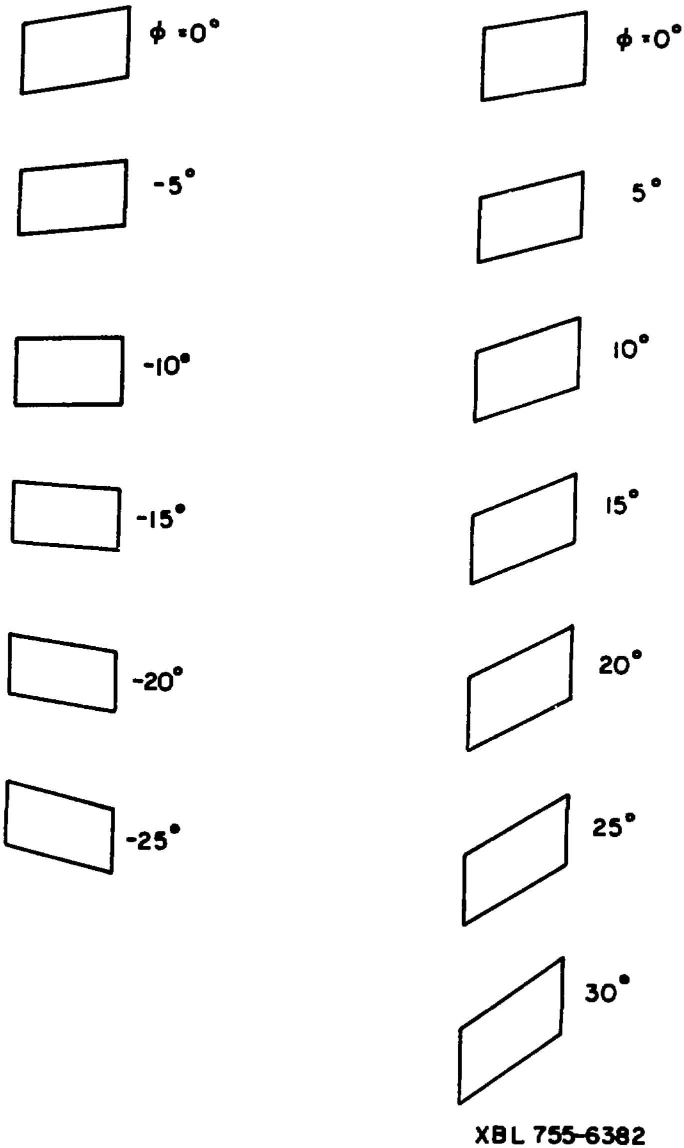

Fig. 21

XBB 755-3978

Fig. 22

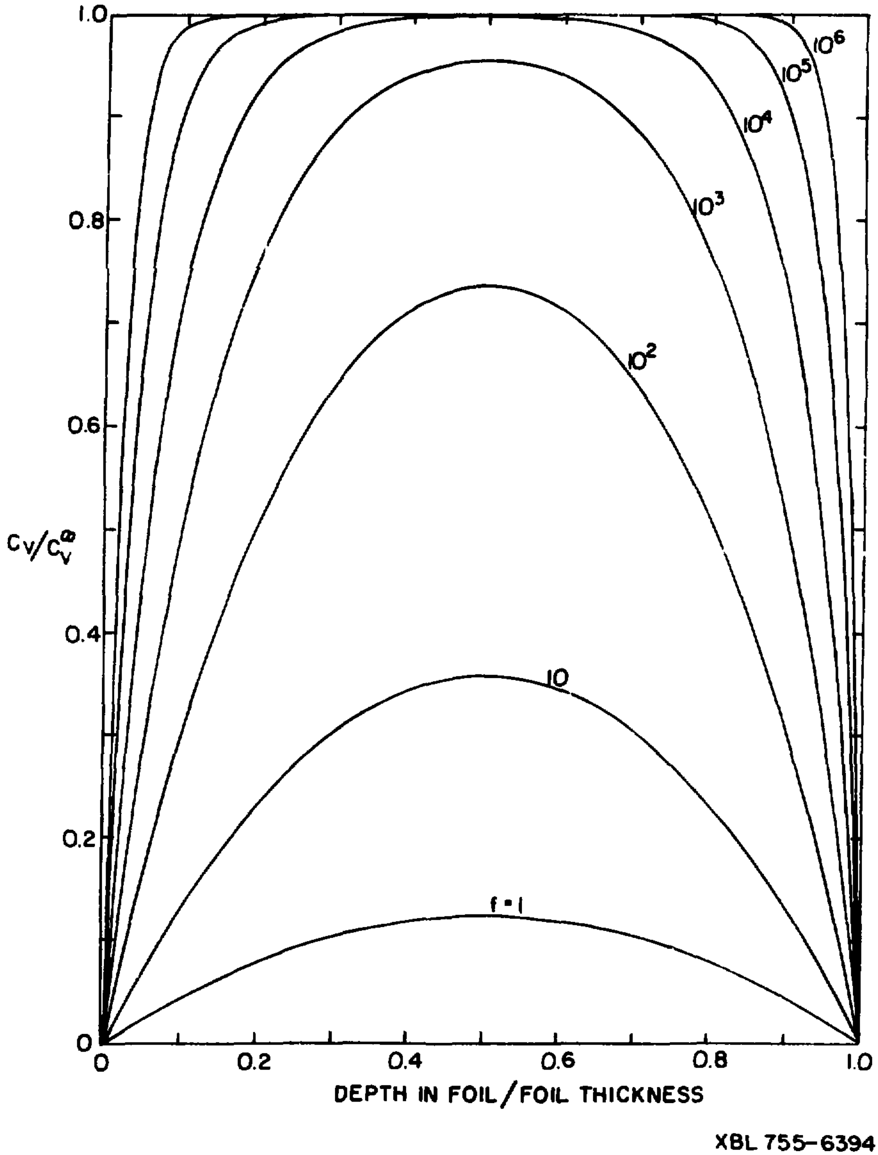
1.0
0.8
0.6
0.4
0.2
0
0
0.2
0.4
0.6
0.8
1.0
C_V/C_V^∞
DEPTH IN FOIL/FOIL THICKNESS
f = 1
10
10^2
10^3
10^4
10^5
10^6
XBL 755-6394

Fig. 23

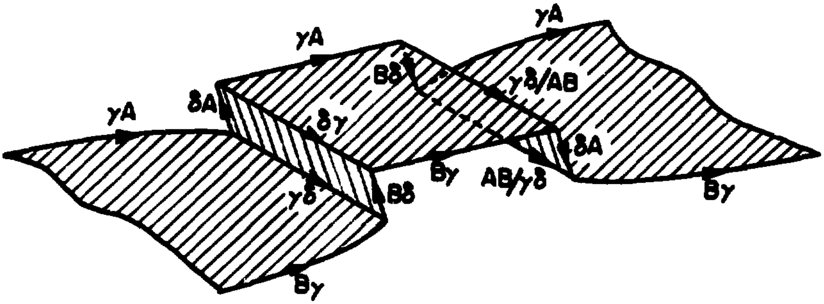

a

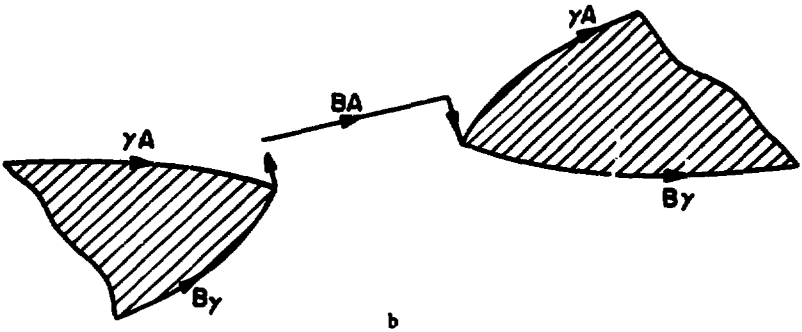

b

XBL755-6383

Fig. 24

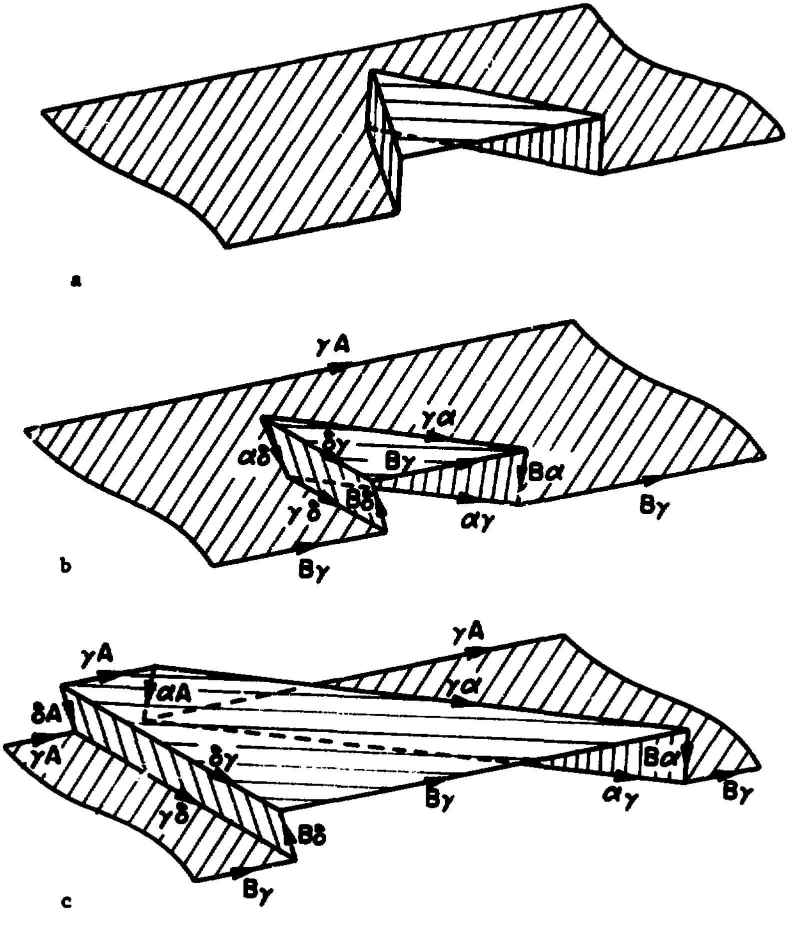

XBL755-6387

Fig. 25

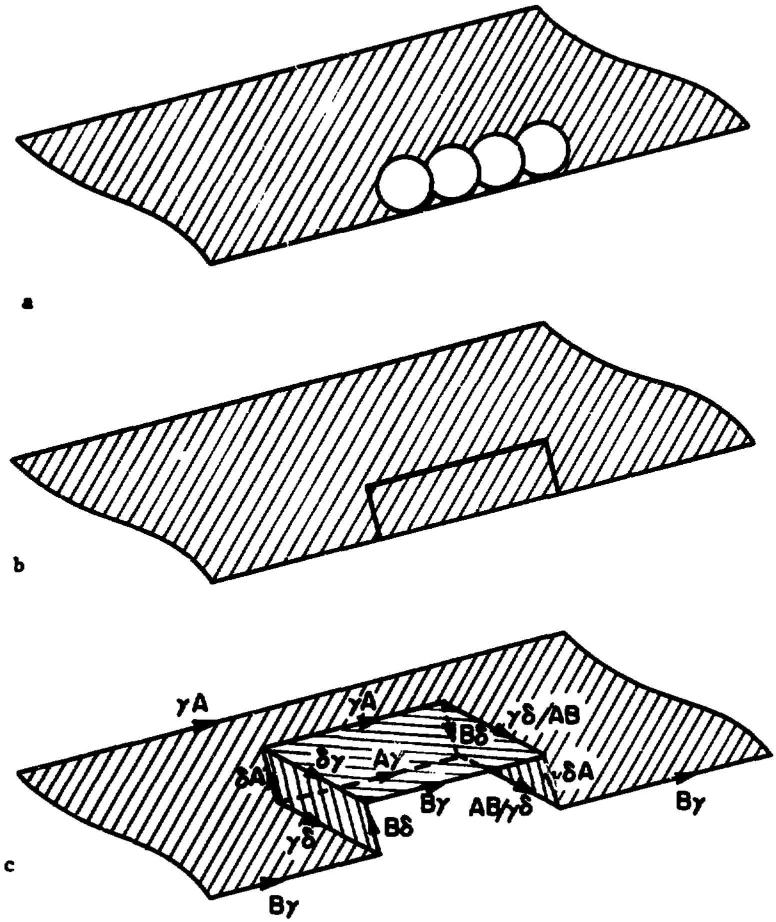

XBL 755-6386

Fig. 26

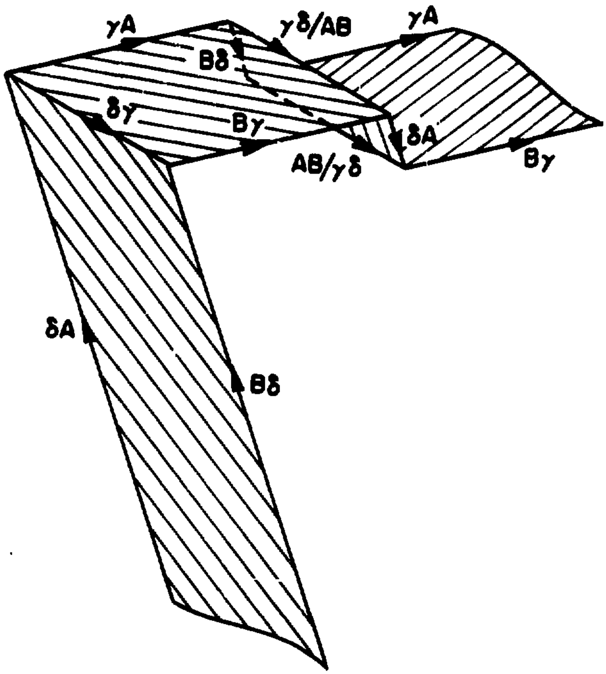

XBL755-6388

Fig. 27